Universität Rostock
Traditio et Innovatio

Leibniz Institute for Baltic Sea Research Warnemünde
IOW

A one-dimensional model for deep-water dependencies in the Baltic Sea

Diploma Thesis

Lennart Schüler

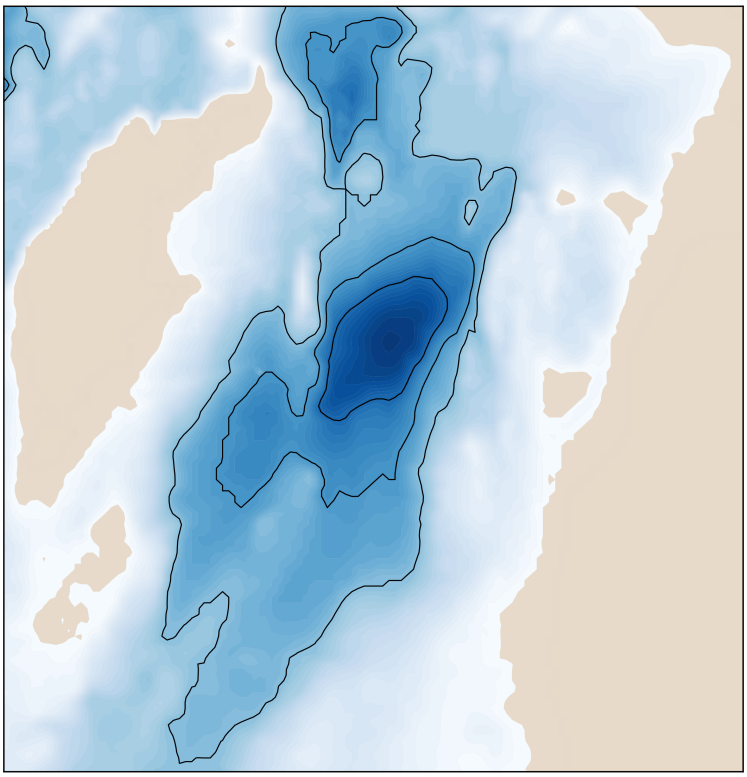

A one-dimensional model for deep-water dependencies in the Baltic Sea

Diploma Thesis

at the
Leibniz Institute for Baltic Sea Research
Department of Physical Oceanography and Instrumentation

submitted by

Lennart Schüler

Institute of Physics
University of Rostock

Rostock, 4 June, 2012

Supervisor and first Reviewer:	Prof. Dr. Hans Burchard
Second Reviewer:	Dr. Martin Schmidt

Contents

Chapter 1

Introduction

1.1 Motivation

The application of three-dimensional numerical hydrodynamic models for simulating lakes or coastal oceans is widespread and computationally affordable on modern high-performance computing systems. These models can account for many effects important for the dynamics of the examined systems including more subtle effects. But often enough it is sufficient to apply more confining assumptions and simplifications, than for these very complex models, in order to, e.g. simplify the model setup, fasten up the computation times, or simplify the model analysis. The simplification of the fully three-dimensional hydrodynamics to a one-dimensional water column model may seem quite rigorous, but the success of many applied one-dimensional water column models proves this wrong. Furthermore the computation time is typically 10^3 to 10^4 times shorter for a one-dimensional model compared to a three-dimensional one (*Jöhnk and Umlauf*, 2001). Thus, vertical one-dimensional models are still an important tool for understanding hydrodynamic processes. There are two cases in which these model types are still quite common. These are, first, sensitivity analyses and model calibrations where a great number of parameters has to be adjusted, which makes it necessary to run a simulation very often with slightly varied parameters. This large number of simulation runs is needed to obtain a sufficiently large parameter space. And second, long time-scale simulations where a simulation time over several decades is wished. Such time-scales are often still not computationally affordable with a three-dimensional hydrodynamic model. In addition, it is very difficult, if not impossible in most situations, to gather fully three-dimensional hydrodynamic data for the initial conditions of such a model and to calibrate and verify it with this data.
Vertical water column models have one crucial disadvantage when simulating inflows from, e.g. rivers flowing into lakes or major Baltic inflows flowing into the sub-basins of the Baltic Sea (*Jöhnk*, 2000). In order to derive the governing equations for a water column model, it is assumed that all variables are homogeneous in the horizontal and that the system is horizontally infinite. This implies that there is no information about the volume of water contained in a modelled basin. But without this knowledge it is impossible to account for the processes triggered by inflows, like the uplift of the residing water masses getting replaced by the newly arriving, inflowing water. One possibility to overcome this cutback is to apply an integration in the horizontal plane of the basin to all the variables. This yields horizontally averaged variables, information about the volume of the basin, and the inclusion of some additional physical effects due to the shape of the basin. Such a

horizontally averaged model will be derived, examined, and implemented into an already existing one-dimensional water column model. This model will then be used to simulate the Gotland Basin in the Baltic Sea including dense bottom currents flowing into this basin which are very important for the dynamics of this basin.

1.2 Outline

In the first chapter, the Baltic Sea will be introduced, as the overall goal of this thesis is to model the Gotland Basin which is a sub-basin of the central Baltic Sea. Not only will the Baltic Sea in general be introduced, but also the Gotland Basin and some of the overall dynamics playing an important role for the hydrodynamic system and also for the ecology of the Baltic Sea. A review of the different applications of one-dimensional modelling of the Baltic Sea closes this chapter.
Some mathematical and physical tools and theories, needed to understand later chapters, will shortly be introduced in chapter 2. Furthermore, the already existing numerical model, which was extended for this thesis, will be summarised.
With the foundation of chapter 2, new, horizontally averaged transport equations are derived and an analytical solution is found in chapter 3. These horizontally averaged equations give the opportunity to include inflows. In order to include inflows, being prescribed far upstream, an entrainment model is introduced. Next, some criteria are listed to objectively determine if the assumption of one-dimensionality is justified for a certain basin. Finally, the discretisation and implementation of the horizontally averaged transport equations is presented.
In chapter 4 the results of this work are presented and analysed. The model derived in the previous chapter is tested against an analytical solution. The results of an idealised model setup to test the computation of inflows is discussed, the results from an alternative discretisation are summarised, and finally the simulation of the Gotland Basin with realistic forcing is described and discussed.
A summery of the previous chapters is given in chapter 5 together with the conclusions of this work.

1.3 The Baltic Sea

The Baltic Sea is a brackish inland sea. The only connection to the open ocean is through the Kattegat and Skagerrak. The water exchange between the Baltic Sea and the open ocean is constrained by shallow and narrow straits south of the Kattegat. From these straits on, the Baltic Sea stretches out to the east in form of several sub-basins linearly aligned as shown in figure 1.1b as a transect along the red line shown in figure 1.1a. The surface salinity decreases from about 25 psu (practical salinity unit, sea *IOC et al.* (2010) for an explanation) at the transition area between the Baltic Sea and the North Sea at the Kattegat to values as low as 5 psu in the far east of the Baltic Sea in the Gulf of Bothnia (*Reissmann et al.*, 2009). This horizontal salinity gradient is mainly due to the humid climate and the large drainage area of the Baltic. The river discharge is so large that more brackish water flows out of the Baltic Sea into the North Sea than saline water flows in from the North Sea. Namely, about $436\,km^3$ of river water discharges into the Baltic per year. Additionally, $224\,km^3$ of water coming from precipitation add to the total water budget. Coming from the North Sea, nearly $500\,km^3$ of highly saline water flows into the Baltic. These three constituents adding to a positive water budget get balanced by $184\,km^3$ evaporating water and a surface water outflow into the North Sea of $947\,km^3$ (*HELCOM*, 1993). However, the saline inflows coming from the North Sea usually do not reach any further than the belts and the Øresund, because the free exchange of water gets hindered by these very narrow and shallow topographical features (*Matthäus and Franck*, 1992). Significant inflows of saline water from the North Sea only occur sporadically and under special meteorological conditions. These inflow events will be further examined later in this section. The surface water is separated from the deeper water by a permanent halocline, which is the part of the water column where the salinity gradient is the steepest. Its depth varies throughout the Baltic Sea. In the Arcona Basin it is situated at about 35 m to 40 m and in the Eastern Gotland Basin it reaches depths of up to 70 m to 90 m depth (*Stigebrandt*, 1987). Thus, processes driven by the atmosphere (e.g. cooling and mixing) do not affect water below this interface which also means that oxygen from the oxygen-rich surface water cannot reach the deeper parts of the Baltic. This implies that deep water can only be renewed by strong inflows of dense water spreading out from the North Sea along the sea bed. The renewal of the deeper water masses plays an important role for the ecology of the Baltic Sea, as during stagnation periods, when no strong inflows occur, the salinity and in particular the oxygen concentrations decrease below the halocline. Furthermore, the concentrations of phosphate and nitrate increase, which can cause high concentrations of hydrogen sulphide (*Matthäus and Franck*, 1992). Under these conditions no higher forms of life can exist.

1.3.1 The Gotland Basin

The Gotland Basin is divided into several sub-basins. This thesis concentrates on the Eastern Gotland Basin, which is the largest basin of the Baltic Sea with respect to the total volume. The bathymetry of the Gotland Basin can be seen in figure 1.2. It is located to the east of the island of Gotland and belongs to the Baltic Proper situated at 57.3 N, 20.08 E in the geographic coordinate system. The basin has a total depth of about 250 m and is enclosed up until a water depth of approximately 140 m (*Seifert et al.*, 2001). At this depth, it is connected to the Bornholm Basin to the west and to the Åland Sea in the north (*Reissmann et al.*, 2009). Only the strongest inflows reach the Gotland

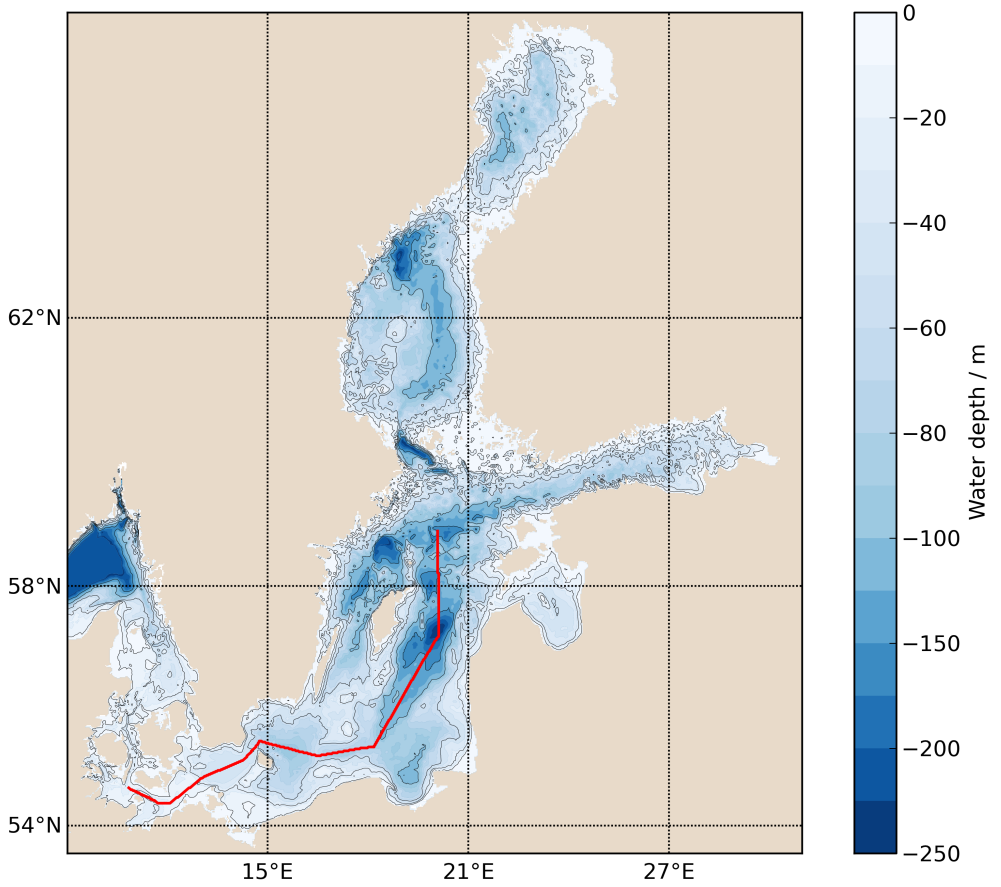

(a) The bathymetry of the Baltic Sea. The red line indicates the transect shown in figure 1.1b (*Seifert et al.*, 2001).

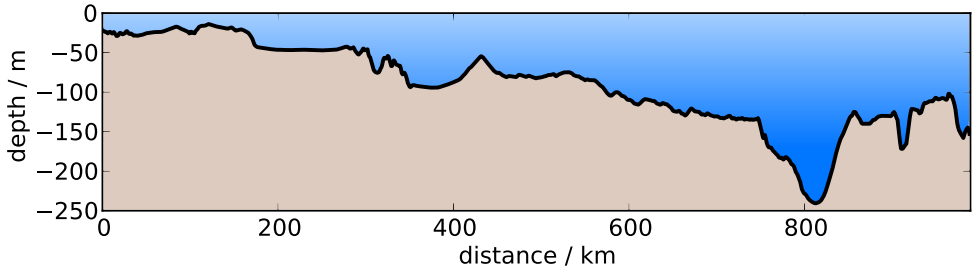

(b) The bathymetry of the Baltic Sea showing the different sub-basins at a transect following one of several pathways of the inflows.

Figure 1.1: A map of the Baltic Sea.

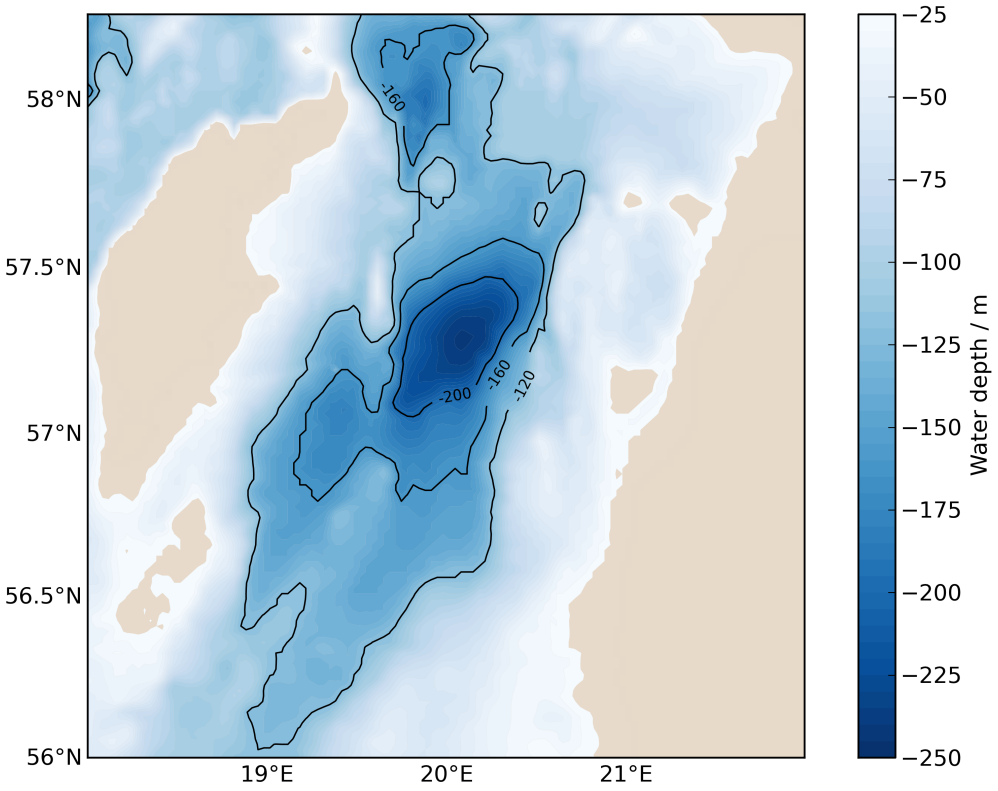

Figure 1.2: The bathymetry of the Gotland Basin.

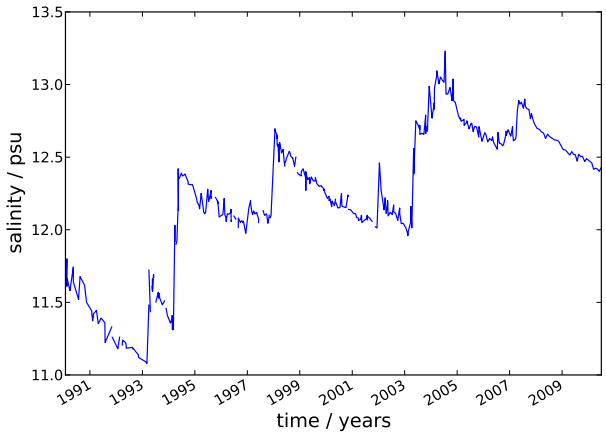

Figure 1.3: The salinity in the Gotland Basin in 200 m depth. The dynamics are mainly influenced by strong, sporadic inflow events, which increase the salinity significantly, followed by stagnation periods of up to ten years where the salinity slowly decreases.

Basin and also end here. Figure 1.3 shows the gradual decline of salinity over stagnation periods and the sporadic inflow events in a depth of 200 m in the Gotland Basin. It can be seen that the inflow events raise the salinity significantly.
The Baltic Sea Tracer Release Experiment (BATRE) (*Holtermann et al.*, 2012; *Holtermann and Umlauf*, 2012), which started in 2007, investigated deep water mixing rates and mixing processes in the Eastern Gotland Basin. The cruises to the basin started in September 2007, when an inert tracer gas, namely CF_3SF_5, was injected at about 200 m depth. The following spreading of the tracer was investigated during several cruises until February 2009. It was found that basin-scale vertical mixing rates were of the order of $10^{-5}\,\mathrm{m^2 s^{-1}}$, however the interior vertical diffusivities were one order of magnitude smaller. From this finding, the conclusion was derived that the vertical transport works in a way that after spreading isopycnically and reaching the lateral boundaries the tracer gets mixed very rapidly vertically by boundary mixing and spreads in different depths isopycnically back again towards the basin interior. These complex processes often get parameterised as an immediate effective vertical mixing, completely neglecting that beneath the halocline the main contributor to vertical mixing is by far the boundary mixing.

1.3.2 Major Baltic inflows

The Baltic Sea is only connected to the oceans through the Kattegat. Here, the surface water typically has a salinity of 15 psu to 25 psu. The bottom water in the Kattegat can reach salinity values as high as 30 psu. In contrast to these high values, the central Baltic Sea has surface salinities of about 8 psu (*Stigebrandt*, 2001). Despite this strong horizontal salinity gradient only small amounts of saline North Sea water reach the inner Baltic Sea under normal meteorological conditions due to the topographical constraints in the transition area between the North Sea and the Baltic Sea (*Matthäus and Franck*, 1992). But two very different meteorological conditions can cause inflows which carry significant amounts of North Sea water into the inner Baltic Sea. These so-called major Baltic inflows occur irregularly. They have been observed from several times a year to only once a decade. During the years from 1897 to 1976 about one major inflow event per year was observed (*Matthäus and Franck*, 1992). From this time on the frequency of the events has decreased to about once every decade (*Matthäus et al.*, 2008).
In order to estimate the relative intensity of inflows, *Matthäus and Franck* (1992) found an empirical equation which takes the duration of an inflow k and the mean salinity S_p of the inflow into account:

$$Q = 50 \left(\frac{k/\,\mathrm{s} - 5}{25} + \frac{10^3 S_p - 17}{7} \right) . \tag{1.1}$$

The formula was slightly modified to take the units of measurement correctly into account. Based upon this definition, an inflow lasting for five days with a salinity of 17 psu has the intensity index of $Q = 0$, which is the least intense inflow being categorised as a major Baltic inflow. Whereas the strongest ever observed inflows lasting as long as 30 days with a salinity of up to 24 psu are classified as $Q = 100$.
Up until recent years it was believed that the pathways of these inflowing dense bottom currents are determined by a balance between the Coriolis force and pressure gradient forces. Thus, they where assumed to be geostrophic flows, with other forces like friction forces acting at the bottom or at the interface of the different water masses only playing a minor role (*Liljebladh and Stigebrandt*, 1996). This behaviour would mean that after the

water masses have passed the Darss and Drogden Sills they cyclonically move along the rims of the Arcona Basin (*Lass and Mohrholz*, 2003). By permanent leakage through the Bornholm Channel north of Bornholm the water moves onwards into the Bornholm Basin. But recent studies, like numerical modelling studies performed by *Burchard et al.* (2005); *Lass et al.* (2005); *Burchard et al.* (2009) and observations performed by *Sellschopp et al.* (2006); *Umlauf et al.* (2007) seem to contradict the cyclonical spiralling of water masses in the Arcona Basin. If frictional forces would only play a minor role in the dynamics of the dense bottom currents, then the pathway of the flow should go along the west of Kriegers Flak, but instead, only a small fraction of the plume follows this pathway and most of it flows along the northern slope of Kriegers Flak. The two separated currents rejoin again south-east of Kriegers Flak and move further along into the eastern part of the Arcona Sea.
Looking at the inflows further in the east, *Meier et al.* (2006) found out that outflows from the Bornholm Sea over the Słupsk Sill, resulting from major Baltic inflows, are highly variable, whereby these variabilities can be separated into three different regimes: "(1) a simple eastward downstream flow when the level of the dense water west of the sill was higher than the level east of the sill, (2) an eastward overflow with a large southward off-set of the dense water core, and (3) bilateral (eddy like) motion above the sill when the salinity gradients north and south the sill were directed oppositely."

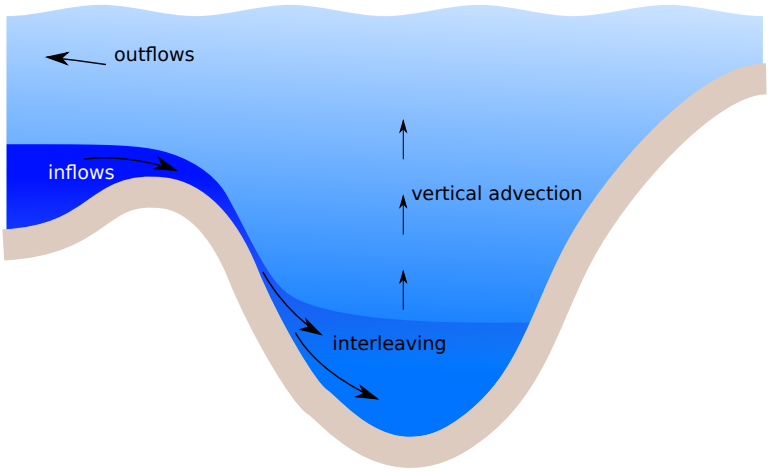

Figure 1.4: The basic dynamic processes causing the ventilation of the deeper parts of the Gotland Basin.

If an inflow reaches the Gotland Basin, it interleaves at the appropriate depth which means at the depth where the residing water has the same density as the inflowing water. The whole water mass sitting on top of the water being renewed gets pushed upwards where it finally ends as a brackish outflow into the North Sea. Figure 1.4 visualises these processes. This estuarine circulation is known as the Baltic Sea counterpart to the oceanic deep convection processes (*Reissmann et al.*, 2009) and is called the Baltic haline conveyor belt.
Lass and Mohrholz (2003) have identified three main mixing mechanisms of bottom currents in the Baltic Sea. The plume can be mixed with the ambient water by wind induced entrainment, but only in the proximity of shallow sills. It can also be mixed by differential advection, which contributes most to mixing and the third mechanism is shear induced entrainment. Differential advection means that two water masses at different depths ad-

vect in different directions or at different velocities.
The causes of the major Baltic inflows can be divided into two fundamentally different ones, namely, into barotropic and baroclinic inflows, which will both be introduced briefly in the following.

Barotropic inflows

A so-called barotropic inflow can occur if strong easterly winds last for typically at least 20 days and after this period turn to the opposite direction and last for at least another five days. These conditions can occur between end of August and end of April (*Matthäus and Franck*, 1992). On the one hand, the strong easterly winds cause a very well-mixed water column in the transition area between the North Sea and the Baltic Sea. And on the other, they lower the sea level in the Baltic Proper by a few 10 cm (*Reissmann et al.*, 2009). If the following westerly winds can push the North Sea water through the belts and the Øresund and across the Darss and Drogden Sills, it interleaves and mixes with the Baltic Sea water in the Arcona Basin. If the density of the North Sea water is higher than the water in the subsequent basins, it can reach as far as the Gotland Basin and replace deep water there. It takes at least three month for an inflow to reach the Gotland Basin (*Hagen and Feistel*, 2001; *Feistel et al.*, 2003; *Hagen and Feistel*, 2004). Typically such an inflow event transports 200 km^3 of water and 2 Gt of salt into the Baltic Sea. In winter and spring this water is oxygen-saturated and contains typically 1 Mt of oxygen reventilating the Baltic Sea (*Reissmann et al.*, 2009).

Baroclinic inflows

So-called baroclinic inflows are driven by baroclinic pressure gradients, especially by horizontal salinity gradients. These gradients appear during prolonged calm wind conditions which usually occur during late summer. Without winds, which induce mixing throughout the water column, a strong stratification develops at the transition area between the North Sea and the Baltic Sea with salinities of over 30 psu in the deeper layers. These high concentrations cause the deeper water layers to flow into the Baltic Proper forced by horizontal salinity gradients. Because of the strong stratification and the absence of winds in the transition area no oxygen can be transported from the surface to the deeper parts of the water column (*Feistel et al.*, 2004a). This means that the water, which can potentially be transported into the Baltic Proper, is oxygen-deficient. These inflows import salt into the Baltic Sea together with a net water volume export. Although the imported water is oxygen-deficient it ventilates the deep Baltic basins by entrainment (*Feistel et al.*, 2004b).

1.4 A review of one-dimensional Baltic Sea modelling

Five different papers will be summerised in this section ordered chronologically. The model used, the investigated topics, and the conclusions drawn will be presented.
Omstedt (1987) used four one-dimensional models of the Kattegat, the Belt Sea, the Øresund, and the Arkona Basin coupled by parameterised in- and outflows between connected regions. For the turbulence modelling a k-ϵ-model was used. The forcing was done with actual meteorological and hydrological observations. Together with these observations, the water cooling at the entrance of the Baltic Sea was investigated. From these observations it was concluded that outflows from the Baltic have an important effect on the

autumn cooling in a way that the cooling is associated with outflowing brackish water from the Arcona Basin. Whereas, periods of interrupted cooling are associated with inflowing saline water from the Kattegat. Furthermore, the applied model reproduced the trends of cooling, derived from the observations, in a satisfying way. From this success, the conclusion was drawn that a one-dimensional model can be used as a good starting point for modelling surface water cooling. This conclusion holds even in such complex topographical areas as the entrance area of the Baltic Sea. The main factor for the successful reproduction of observations seems to be how well the turbulent processes and the energy exchange at the air-sea interface are modelled. In addition, the subdivision of the simulated areas and the parameterisation of the water exchange between these basins are important, too.

Stigebrandt (1987) used a one-dimensional model to simulate the Baltic Proper with a focus on the deep water dynamics. The presented model is horizontally integrated which takes hypsographic effects into account. For calculating the properties of the mixed layer, a seasonal pycnocline model derived by *Stigebrandt* (1985) was utilised. In order to calculate the turbulence, it was assumed that the horizontally averaged eddy-diffusivity is proportional to the inverse Brunt-Väisälä frequency $\kappa \propto N^{-1}$. Inflows, including major Baltic inflows, moving along the Baltic Sea as dense bottom currents were prescribed upstream in the Arcona Basin and were modelled by a simple entrainment model also being derived by *Stigebrandt* (1987). The forcing was done by partially prescribing observed atmospheric data and partially by prescribing synthetic values of, e.g., the daily wind speed or the salinity and the temperature of the inflowing water in the Arcona Basin. The synthetic data was generated according to statistical properties of observed data. This had to be done, because no observations were available with sufficient time resolution. The use of synthetically generated data means that a direct month-to-month comparison of model results with observed data is not possible, but nevertheless statistical properties like mean values can be compared. The model reproduced the vertical stratification of the Baltic Proper in a realistic way, with the halocline being at about 60 m depth and a strongly stratified water column beneath it. It was concluded that the inflows have a major influence on the stratification. But for predicting hydrological changes in the Baltic, caused, for example, by a change in the freshwater balance, the presented model is not sufficient, because it relies on prescribed values for the characteristics of the inflows.

Stigebrandt and Wulff (1987) presented a model for the dynamics of nutrients and oxygen in the Baltic Proper. The model, computing the hydrological dynamics, was the same as in *Stigebrandt* (1987) which also includes the use of synthetic data forcing the simulation. The biogeochemical cycle was modelled by only considering nitrogen. With this approach, not all processes could be modelled, like nitrogen fixation which is controlled by the nitrogen-phosphorous ratio. In order to overcome this shortcoming, these processes were included through external sources. The biogeochemical model, together with the hydrodynamical model, could generate the characteristics of oxygen and nitrogen distributions in a rough but satisfying way.

A few years later *Omstedt* (1990) greatly enhanced his model from 1987 and used this new model to simulate the whole Baltic Sea. In total, 13 one-dimensional models were used for the simulation. The subdivision of the Baltic was done according to natural restrictions, such as geometrical or dynamic restrictions. The model was forced by meteorological data and by sea level data at the Skagerrak. The flows from one basin to the next where first categorised into either river inflows, barotropic flows, or baroclinic flows and then they were parameterised. The winter of 1986/87, being especially severe, was chosen to be sim-

ulated to test the model against observations. The model did not incorporate an ice model and the water temperature was only kept at the freezing point, when the water was cooled strong enough. This simplification neglects two important effects on the heat budget of the water. First, ice covering water protects it from further heat loss and second, energy is needed to melt it again. Thus deeper parts of the water column should be too cold in the simulation and the spring warming should be too fast. However, the simulation results were surprisingly good as they could reproduce the cooling and warming quite well.
Axell (2002) used a one-dimensional model to find suitable parameterisations of unresolved turbulence which sources could be the breaking of internal waves or Langmuir circulations, respectively. The Eastern Gotland Basin was simulated. The vertical transport equations were not horizontally averaged, but the hypsographic function was used to calculate the effects of inflows which were calculated based on the entrainment model derived by *Stigebrandt* (1987). For the turbulence calculations, a k-ϵ-model was used, with Langmuir circulations being taken into account for by additional source terms for the turbulent kinetic energy in the surface mixed layer. The model results were satisfying although the modelling of the deep inflows is notoriously difficult, not only because of the relatively poor temporal and spatial resolution of observations of these inflows. Finally, it was concluded that Langmuir circulations and the breaking of internal waves are important when modelling the Baltic Sea.
A coupled physical-biogeochemical modelling system was presented by *Burchard et al.* (2006). The General Ocean Turbulence Model (GOTM) was used for the computations of the hydrodynamics. It includes state-of-the-art turbulence closures. The two-way coupling to biogeochemical models is flexible, but a few restrictions were made. They have to be Eulerian-type of models, where all state variables are concentrations. Because of the numerous different turbulence closure models and the various biogeochemical models which can be combined together and the fast computation times in comparison with fully three-dimensional models this modelling system is predestined for the use as a work bench for comparing different physical or biogeochemical parameters or for sensitivity analyses. Applications of this modelling system were presented for the North Sea and for the Baltic Sea. For the Baltic Sea simulation, the salinity was nudged to observational data with a time scale of two days, because the inflows could not be modelled without the inclusion of the hypsography. The observations from both seas could be reproduced qualitatively. But the results of the biogeochemical model strongly depend on the chosen turbulence closure. Another problem is the uncertainty about several ecosystem parameters. The conclusion was drawn that one-dimensional water column models can typically not be used for quantitatively predicting ecosystem dynamics. But for simple studies or for model development in a broad sense the flexibility and the fast computation times make this model appealing.

Chapter 2

Methods

2.1 Mathematical tools

In this section the tools and theories needed to understand the later chapters will be introduced. The information presented here is based on *Kundu and Cohen* (2008) and *Pope* (2000).
First, Reynolds' transport theorem will be introduced briefly, as this theorem is not only crucial for the derivation of the Navier-Stokes equations, but it is also important for the derivation of the horizontally averaged transport equations being derived later. Next, the Navier-Stokes equations, as the governing equations of fluid dynamics, will be repeated as a foundation for the following section, which introduces the Reynolds-averaged Navier-Stokes equations (RANS). These RANS equations are the starting point for many turbulence models, of which one class of turbulence models will finally be summarised.

2.1.1 Reynolds' transport theorem

The well-known Gauss' theorem generalises the fundamental theorem of calculus and states that, for a vector $\vec{F}$,

$$\int_V \nabla \cdot \vec{F} \, \mathrm{d}V = \oint_{\partial V} \vec{F} \cdot \vec{n} \, \mathrm{d}A \, , \tag{2.1}$$

where V is an arbitrary, but simply connected volume, bounded by the surface ∂V. Geometrically, this formula states that the outward flux through the surface ∂V is equal to the volume integral of the divergence of a vector. But this theorem is only valid for volumes which are constant and do not change, e.g. with time. For only one dimension the solution to this problem is called Leibniz' Rule:

$$\frac{\mathrm{d}}{\mathrm{d}t} \int_{a(t)}^{b(t)} F(x,t) \, \mathrm{d}x = \int_{a(t)}^{b(t)} \frac{\partial F(x,t)}{\partial t} \, \mathrm{d}x + \frac{\mathrm{d}b}{\mathrm{d}t} F(b,t) - \frac{\mathrm{d}a}{\mathrm{d}t} F(a,t) \, . \tag{2.2}$$

This rule can be generalised to three dimensions by means of continuum mechanics:

$$\frac{\mathrm{d}}{\mathrm{d}t} \int_{V(t)} \vec{F}(\vec{x},t) \, \mathrm{d}V = \int_{V(t)} \frac{\partial \vec{F}(\vec{x},t)}{\partial t} \, \mathrm{d}V + \oint_{\partial V(t)} \vec{F} \, \vec{u}_A \cdot \vec{n} \, \mathrm{d}A \, , \tag{2.3}$$

where $V(t)$ is a volume which can move over time and which is bounded by the moving surface $\partial V(t)$. The velocity of the boundary is denoted with $\vec{u}_A$. If a volume always contains the same fluid particles, it is a material volume which is exactly the case, when the velocity of the fluid $\vec{u}$ and the velocity of the bounding surface are equal: $\vec{u} = \vec{u}_A$. If $V(t)$ is a material volume, equation (2.3) becomes

$$\frac{\mathrm{d}}{\mathrm{d}t} \int\limits_{V(t)} \vec{F}(\vec{x}, t)\, \mathrm{d}V = \int\limits_{V(t)} \frac{\partial \vec{F}(\vec{x}, t)}{\partial t}\, \mathrm{d}V + \oint\limits_{\partial V(t)} \vec{F}\vec{u} \cdot \vec{n}\, \mathrm{d}A \tag{2.4}$$

and is called Reynolds' transport theorem.

2.1.2 Navier-Stokes equations

The governing equations for all known fluid dynamics are the Navier-Stokes equations. These equations are very general, but no analytical solution is known and, because most often the ocean dynamics are important on length and time scales of several orders of magnitude, direct numerical simulations are only applicable in special cases. Thus, physically motivated, simplifying assumptions have to be made. For geophysical ocean mechanics the Boussinesq assumption is widely applied. It assumes that the density differences are so small that they can be neglected in every term, except for the buoyancy term. With the Boussinesq assumption made and set in a rotating frame the Navier-Stokes equations can be written as

$$\frac{\partial \vec{u}}{\partial t} + \vec{u} \cdot \nabla \vec{u} - \nu \nabla^2 \vec{u} + 2\vec{\Omega} \times \vec{u} = -\frac{1}{\rho_0} \nabla p + \frac{\rho}{\rho_0} \vec{g}\,. \tag{2.5}$$

Here, $\vec{u}$ is the velocity, $\vec{\Omega}$ is earth's rotation, with $2\vec{\Omega} \times \vec{u}$ being the Coriolis term, ρ is the density with a constant reference density ρ_0 and ν is the kinematic viscosity, also known as the diffusivity of momentum. With the Boussinesq assumption applied, the continuity equation simplifies to

$$\nabla \cdot \vec{u} = 0\,. \tag{2.6}$$

2.1.3 Reynolds-averaged Navier-Stokes equations

Due to the deterministically chaotic nature of turbulent flows, it is not only impossible to predict the evolution of a dynamic turbulent system, but most often this is not even wished, because even the slightest change in the initial conditions could lead to totally different result. Instead, mean characteristics of the fluid can be more interesting, like the distribution of the mean velocity or the temperature. If a system is stationary, the time mean

$$\langle u \rangle^{t_0} = \frac{1}{t - t_0} \int\limits_{t_0}^{t} u(t')\, \mathrm{d}t' \tag{2.7}$$

could be used to extract the averaged information of interest. The index t_0 in $\langle u \rangle^{t_0}$ indicates that the time mean depends on the initial conditions of a system, which means that without knowing the exact and complete initial conditions $\langle u \rangle^{t_0}$ cannot be calculated.

Thus, we postulate that

$$\langle u \rangle = \lim_{t \to \infty} \langle u \rangle^{t_0} \tag{2.8}$$

exists and is independent of the initial conditions. This postulate is a special form of the ergodic hypothesis. But even with this postulate, in principle, the system would have to be measured for an infinitely long time to calculate the time mean. Accordingly, the concept of the ensemble average has to be introduced. An ensemble is a collection of imaginary systems, all macroscopically identical copies of the actual, real system being examined. Each member of this collection implements a possible microscopic state which has the same macroscopic physical properties as the real system. The ensemble average is then

$$\langle u \rangle(t) = \frac{1}{N} \sum_{i=1}^{N} u^i(t) \ , \tag{2.9}$$

with N being the number of microscopic realisations of the macroscopic state.
In laboratory experiments or in numerical simulations a relatively small number of repetitions of the same experiment under the same initial conditions can be used to apply the true ensemble average (2.9). But when observing geophysical flows, the experiments cannot be repeated under the same conditions again. Thus, different kinds of filtering procedures have to be applied. These filters could be time filters or spatial filters, but, except for very special cases, they are not equivalent to the ensemble average.
Osborn Reynolds used this ensemble average to decompose observables of a turbulent field into a mean part and a fluctuating part to simplify the Navier-Stokes-Equations. The so-called Reynolds decomposition is

$$u = \langle u \rangle + u' \ , \tag{2.10}$$

with $\langle u \rangle$ being the ensemble average and u' being the fluctuations which is defined as

$$u' := u - \langle u \rangle \ , \tag{2.11}$$

and which vanishes under the ensemble average:

$$\langle u' \rangle = 0 \ . \tag{2.12}$$

Following so-called Reynolds rules apply for the averaging which are important for deriving the later following equations:

1. Linearity: $\langle u + \lambda v \rangle = \langle u \rangle + \lambda \langle v \rangle$
2. Commutation of derivatives and the averaging: $\langle \frac{\partial u}{\partial x} \rangle = \frac{\partial}{\partial x} \langle u \rangle$
3. Idempotence: $\langle \langle u \rangle \rangle = \langle u \rangle$
4. Product average: $\langle u \langle v \rangle \rangle = \langle u \rangle \langle v \rangle$

The Reynolds decomposition can now be applied to the continuity equation. For simplicity the Einstein notation will be used from now on.

$$\frac{\partial}{\partial x_i}(\langle u_i \rangle + u_i') = 0 \tag{2.13}$$

Averaging this equation results in

$$\frac{\partial \langle u_i \rangle}{\partial x_i} = 0 \tag{2.14}$$

and subtracting equation (2.14) from equation (2.13) yields

$$\frac{\partial u_i'}{\partial x_i} = 0 \; . \tag{2.15}$$

Equations (2.14) and (2.15) show that not only the mean flow, but also the fluctuations are non-divergent.
If the Reynolds decomposition is inserted into the Navier-Stokes equations (2.5), the equations get averaged, and the continuity equations (2.14) and (2.15) are applied, then the so-called Reynolds-averaged Navier-Stokes equations (RANS) are obtained:

$$\frac{\partial \langle u_i \rangle}{\partial t} + \frac{\partial}{\partial x_j}\left(\langle u_i \rangle \langle u_j \rangle + \langle u_i' u_j' \rangle - \nu \frac{\partial \langle u_i \rangle}{\partial x_j} \right) + 2\epsilon_{ijk}\Omega_j \langle u_k \rangle = -\frac{1}{\rho_0}\frac{\partial \langle p \rangle}{\partial x_i} + \frac{g_i}{\rho_0}\langle \rho \rangle \tag{2.16}$$

Comparing this equation to the original Navier-Stokes equations in index notation:

$$\frac{\partial u_i}{\partial t} + \frac{\partial}{\partial x_j}\left(u_i u_j - \nu \frac{\partial u_i}{\partial x_j} \right) + 2\epsilon_{ijk}\Omega_j u_k = -\frac{1}{\rho_0}\frac{\partial p}{\partial x_i} + \frac{g_i}{\rho_0}\rho \; , \tag{2.17}$$

we can see that there are only two differences between these equations. The RANS equations, describing the dynamics of a mean velocity field, only contain averaged variables, instead of the instantaneous observables in the original Navier-Stokes equations. And the correlation between different fluctuating velocities $\langle u_i' u_j' \rangle$ has appeared as an additional transport term in the RANS equations. This term is also known as the Reynolds stress tensor. Dynamic equations for $\langle u_i' u_j' \rangle$ can be derived which are known as the second moment equations, but they include third moment terms, like $\langle u_i' u_j' u_k' \rangle$. For these third moments too, dynamic equations can be found, but they include terms of fourth order and so on. This dilemma is known as the turbulence closure problem.

2.1.4 Turbulence closure

By introducing empirical parameterisations, the RANS equations can be closed and, depending on which statistical moments are used to close the system, the closure models are called first-moment, second-moment or higher-moment closure models. A few prerequisites are introduced in order to understand the closure models.

Eddy viscosity

The eddy viscosity assumption is based on an analogy between the mean flow and the fluctuating flow first described by Boussinesq. For a one-dimensional unidirectional flow $\langle u \rangle = \langle u \rangle(z)$ the total shear stress is

$$\tau = \tau_m + \tau_t = \rho_0 \left(\nu \frac{\partial \langle u \rangle}{\partial x} - \langle u'w' \rangle \right) . \tag{2.18}$$

In analogy to the first term inside of the parenthesis, the turbulent stress is now formulated as

$$-\langle u'w' \rangle = \nu_t \frac{\partial \langle u \rangle}{\partial z} , \tag{2.19}$$

where ν_t is the so-called eddy viscosity. The molecular viscosity ν is a known material property, whereas the eddy viscosity ν_t highly depends on the properties of the flow. It can be many orders of magnitude greater than the molecular viscosity. This eddy viscosity principle can be generalised to three-dimensional flows and can also be made for scalar quantities like the salinity. The introduction of the eddy viscosity cannot close the RANS equations, instead it shifts the problem to finding assumptions with which the eddy viscosity ν_t can be calculated.

The mixing length

With the mixing length approach, Prandtl suggested a parameterisation of the eddy viscosity based on another analogy to molecular diffusion. The kinetic theory of gases shows that the viscosity of a gas is proportional to $\nu \propto a\lambda$, with a being the root mean square velocity of the particles and λ being the mean free path of a particle. For a turbulent fluid this translates to

$$\nu_t = lq , \tag{2.20}$$

where q is a typical velocity scale of turbulence and l is a typical length scale. The task of turbulence modelling is now to find appropriate values for q and l. There are different possibilities to compute these quantities. The turbulent kinetic energy (TKE)

$$k = \frac{1}{2} \langle u_i' u_i' \rangle , \tag{2.21}$$

describing the mean kinetic energy contained in the turbulent field can be related to the velocity scale $k = q^2/2$. A dynamic equation for the turbulent kinetic energy can be derived from the Navier-Stokes equations (2.5):

$$\frac{\partial k}{\partial t} - D = P + G - \epsilon . \tag{2.22}$$

This form of the equation hides a lot of details and only shows which physical processes contribute to the change of k over time, but for this broad overview of turbulence modelling this is sufficient and it will not be described how exactly the terms look like. D contains all transport terms, whereas on the right hand side of the equation all terms describe either sources or sinks of k. P denotes the shear production, which describes the conversion of mean kinetic energy to turbulent kinetic energy and the other way round. The buoyant production G either describes the kinetic energy loss if the turbulence works against a stable stratification of the water column or it describes the gain of turbulent kinetic energy due to unstable stratification. The last term ϵ is the rate of dissipation of turbulent kinetic energy into internal energy. Equation (2.22) plays an important role in modelling turbulence.

Turbulence modelling

There are many different approaches to finding values for the velocity scale q and for the length scale l. Describing even just some of them would go beyond the scope of this thesis. Instead, some of the different approaches will be listed very briefly in order of increasing complexity.

- The most simple models use algebraic relations to compute both q (or k) and l. These models are often too simple to be within a valid assumption for more than only very special cases of flows.
- The so-called one-equation models are more complex than the algebraic models, as k is calculated from the partial differential equation (2.22). The length scale l is again computed from an algebraic relation.
- In the class of the two-equation models not only k is computed from differential transport equations, but also l. There are different variables which can be related to the length scale, for example the rate of dissipation ϵ_{ij}, which results in the well-known k-ϵ-model. These two-equation models are more general than the other two classes of models and may be applied to a broader range of flow situations.

For more information on this topic see e.g. *Speziale* (1991), *Umlauf et al.* (2003), *Umlauf and Burchard* (2005), *Canuto et al.* (2001) or *Pope* (2000).

2.2 The General Ocean Turbulence Model

The General Ocean Turbulence Model (GOTM) is a one-dimensional water column model which can either be used as a stand-alone water column model or as a vertical turbulence closure model, e.g. for a three-dimensional circulation model. It computes the vertical one-dimensional transport equations for salt, heat and momentum. For these calculations, the turbulent fluxes of these quantities have to be calculated. GOTM provides a number of different state-of-the-art turbulence closure models for this (*Burchard and Bolding*, 2001; *Umlauf et al.*, 2005). The physical assumptions made for and the equations solved by GOTM will be shortly introduced here.
The Reynolds decomposition, introduced in section 2.1.3, separates a variable into an ensemble average and into a fluctuating part. This can be expressed as

$$\varphi = \langle\varphi\rangle + \varphi' \,.$$

The variable φ can, e.g. describe a turbulent field. Then the decomposition separates this field into a mean part and into a turbulent part. Only the mean flow equations of GOTM were altered in order to create the lake model, thus only this part will be introduced here. In principle the governing transport equation solved by GOTM is

$$\frac{\partial\langle\varphi\rangle}{\partial t} = \frac{\partial}{\partial z}\left((\kappa_m + \kappa_t)\frac{\partial\langle\varphi\rangle}{\partial z}\right) \tag{2.23}$$

which is a one-dimensional diffusion equation with the eddy viscosity assumption made. Some terms were left out here, for example, in order to compute the heat, a source term

describing the solar radiation would have to be included. In order to derive this equation from the primitive equations, it has to be assumed that all variables are horizontally homogeneous and that the simulation domain has a horizontally infinite size.
It should always be kept in mind that, although one-dimensional water column models use vertical eddy diffusivities for a transport in the vertical and often enough this produces good results, this is not the way vertical transport works in nature. Instead, the vertical transport in a basin is drastically increased by boundary mixing (*Holtermann et al.*, 2012) which means that a tracer in the interior of a basin spreads isopycnically until it reaches the basin boundary where it experiences mixing rates several orders of magnitude greater than in the interior. From the boundary, where the tracer gets mixed into different depth layers, it spreads out again into the interior of the basin at these different depths. These complex processes are parameterised by rather simple vertical diffusivities.

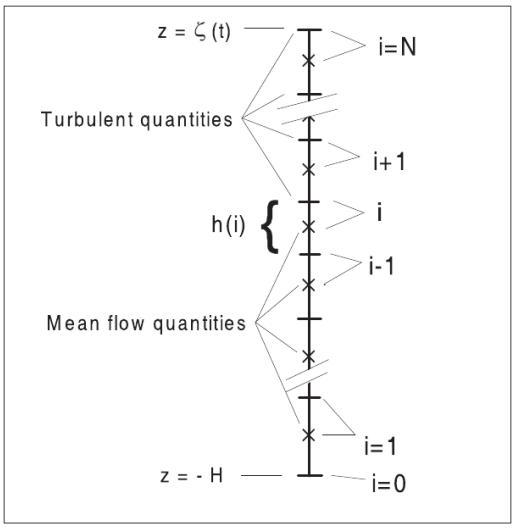

Figure 2.1: The spatial discretisation used by GOTM (from *Umlauf et al.* (2005)).

For the numerical discretisation, the vertical axis is divided into N layers with indices $i = 1, \ldots, N$. These layers have a thickness of h_i, see figure 2.1. The spatial grid is staggered for ease of discretisation of most of the fluxes. The diffusive transport is calculated by a semi-implicit numerical scheme and the advective transport, if it is wished to be calculated too, can be calculated by a choice of different high order numerical schemes. The linear system of equations, resulting from the semi-implicit diffusion scheme, is solved by a simplified Gaussian elimination algorithm. The time stepping is equidistant.
GOTM can be forced by meteorological data like wind, temperature, humidity, and so on. It also incorporates the implications of evaporation and precipitation for the water level change. It can be coupled to biogeochemical models, but introducing this coupling would go beyond the scope of this thesis.
In the following chapter new equations and models will be derived which will be included into GOTM in order to extend the application range of this numerical model.

Chapter 3

The model

In order to realistically model a basin with inflows by using a one-dimensional model, depth-dependent information about the volume of the basin is needed. If an inflow occurs at a certain depth, then the water masses above this depth are pushed upwards. These processes can only be modelled with information about the basin volume. Therefore, new dynamic equations for horizontally averaged variables are derived. They also consider information about the volume of the basin. Following this derivation, an analytical solution is found which can be used to test numerical implementations of the new dynamic equations. Because the flow paths of North Sea water, flowing into the Baltic Sea, are constrained by the Darss Sill and by the Drogden Sill leading to the Arcona Basin, a lot of the measurements about major Baltic inflows have been done here. Moreover, it would be very difficult to estimate the volume flow into the Gotland Basin from measurements done in the vicinity of it as the inflowing water is not constrained to one particular flow path into the basin. Thus, the inflows have to be prescribed at the sills or in the Arcona Basin and the effects of entrainment diluting the dense bottom current need to be modelled with an entrainment model which is also introduced in this chapter.

3.1 Deriving the vertical transport equations

The one-dimensional horizontally integrated vertical transport equation for an arbitrary tracer φ, e.g. salinity will now be derived. The three-dimensional transport equations for a tracer φ, from which this derivation will start, is given by

$$\frac{\partial \varphi}{\partial t} + \vec{u} \cdot \nabla \varphi = \nabla \cdot (\kappa \nabla \varphi) \; . \tag{3.1}$$

The first term describes the change of concentration over time, the second term describes the advective transport, and the third term describes the diffusive transport with $\kappa = \kappa_m + \kappa_t$ being the sum of the molecular and the eddy diffusivity of φ. $\vec{u}$ denotes the advection velocity.
By integrating the transport equation (3.1) in the horizontal, the x and y dependencies of the variables get eliminated and an equation for mean values, only depending on the vertical z axis, is obtained. One thing has to be thought of here. The integration has to be done over a volume and not a plane in order to obtain meaningful expressions as, e.g. density has the unit $\mathrm{kg/m^3}$. Therefore, the integration will be applied in following way:

$$\lim_{\Delta z \to 0} \frac{1}{\Delta z} \int\limits_{V(z)} \mathrm{d}V \ , \tag{3.2}$$

where $V(z)$ is the volume enclosed by the basin, a horizontal plane at the depth z, and a horizontal plane at the depth $z + \Delta z$. If the limit is applied and the integral is computed without an argument, then it yields the total area of a horizontal slice of the basin at the depth z. The area of the horizontal slices at given depths is described by the function $A(z)$ which is the so-called hypsographic function, or shorter the hypsography. See figure 3.1 for a visualisation.

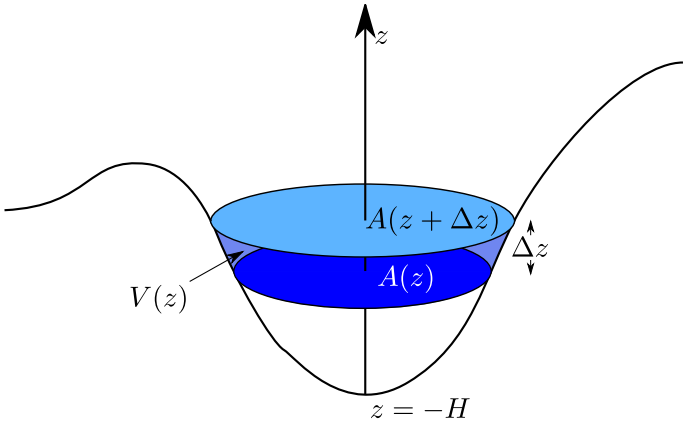

Figure 3.1: A visualisation of the most important geometrical variables for the horizontal integration of the transport equations. $A(z)$ denotes the hypsographical function, V denotes the volume bounded by the basin, the plane of the area $A(z)$, and the plane of $A(z + \Delta z)$.

By applying integration (3.2) to the transport equations (3.1) following expression is found:

$$\lim_{\Delta z \to 0} \frac{1}{\Delta z} \int\limits_{V(z)} \frac{\partial}{\partial t} \varphi(\vec{x}, t) \, \mathrm{d}V =$$
$$\lim_{\Delta z \to 0} \frac{1}{\Delta z} \int\limits_{V(z)} \left\{ \nabla \cdot \left(\kappa(\vec{x}, t) \nabla \varphi(\vec{x}, t) \right) - \vec{u}(\vec{x}, t) \cdot \nabla \varphi(\vec{x}, t) \right\} \mathrm{d}V \ . \tag{3.3}$$

The order of the integral and the time derivative can be swaped on the left hand side of the equation (3.3) according to the simplified Leibniz rule (see chapter 2.1.1). This rule can be applied, because the integration limits are independent of time. Performing this step results in

$$\frac{\partial}{\partial t} \lim_{\Delta z \to 0} \frac{1}{\Delta z} \int\limits_{V(z)} \varphi \, \mathrm{d}V =$$
$$\lim_{\Delta z \to 0} \frac{1}{\Delta z} \int\limits_{V(z)} \nabla \cdot \left(\kappa \nabla \varphi \right) \mathrm{d}V - \lim_{\Delta z \to 0} \frac{1}{\Delta z} \int\limits_{V(z)} \vec{u} \cdot \nabla \varphi \, \mathrm{d}V \ . \tag{3.4}$$

The variable φ on the left hand side of equation (3.4) can be substituted by

$$\bar{\varphi}(z,t) = \lim_{\Delta z \to 0} \frac{1}{\Delta z A(z)} \int\limits_{V(z)} \varphi(\vec{x},t)\,\mathrm{d}V\ , \tag{3.5}$$

which is a horizontally averaged variable for φ using the hypsographic function $A(z)$. It is the goal of this whole derivation to express every variable in this way, as these averaged variables only have a z-dependence and are thus one-dimensional.
The advective term on the right hand side of equation (3.4) can be transformed to a conservative form by means of the incompressibility condition $\nabla \cdot \vec{u} = 0$:

$$\frac{\partial A\bar{\varphi}}{\partial t} = \lim_{\Delta z \to 0} \frac{1}{\Delta z} \int\limits_{V(z)} \nabla \cdot (\kappa \nabla \varphi)\,\mathrm{d}V - \lim_{\Delta z \to 0} \frac{1}{\Delta z} \int\limits_{V(z)} \nabla \cdot (\vec{u}\varphi)\,\mathrm{d}V\ . \tag{3.6}$$

Because A is constant with respect to t, it can be pulled out of the time derivative on the left hand side. In index notation, with the Einstein summation convention applied, equation (3.6) therefore becomes

$$A\frac{\partial \bar{\varphi}}{\partial t} = \lim_{\Delta z \to 0} \frac{1}{\Delta z} \int\limits_{V(z)} \frac{\partial}{\partial x_i}\left(\kappa \frac{\partial \varphi}{\partial x_i}\right)\mathrm{d}V - \lim_{\Delta z \to 0} \frac{1}{\Delta z} \int\limits_{V(z)} \frac{\partial (u_i \varphi)}{\partial x_i}\,\mathrm{d}V\ . \tag{3.7}$$

The integrals on the right hand side of equation (3.7) can be calculated by applying the Reynolds transport theorem in a modified form.
The Reynolds transport theorem, already introduced in chapter 2.1.1, is shortly repeated here:

$$\frac{\mathrm{d}}{\mathrm{d}t} \int\limits_{V(t)} F(\vec{x},t)\,\mathrm{d}V = \int\limits_{V(t)} \frac{\partial}{\partial t} F(\vec{x},t)\,\mathrm{d}V + \oint\limits_{\partial V(t)} F(\vec{x},t)\vec{u}_A \cdot \vec{n}\,\mathrm{d}A\ . \tag{3.8}$$

In this case, F is an arbitrary tensor of any order, V is a simply connected arbitrary volume, which is bounded by the surface ∂V. The vector $\vec{n}$ is normal to the surface ∂V and points outwards. The variable $\vec{u}_A = \left.\frac{\mathrm{d}\vec{x}}{\mathrm{d}t}\right|_{\vec{x} \in \partial V}$ denotes the velocity which the boundary ∂V moves with.
This theorem can be adapted to the current problem in following way. The tensor F is chosen to be of first order and is thus a scalar quantity. It is renamed to F_z. The time t is exchanged with the depth z. This implies that the "speed" of the boundary $\vec{u}_A$ is no longer a change of position over time but over depth with the unit $[\vec{u}_A] = m/m = 1$. The normal vector $\vec{n}$ is replaced by a vector, which lies in the horizontal plane of the hypsography A and is perpendicular to the boundary of A. It is renamed to $\vec{n}_A$. The area of the basin boundary, which is enclosed by the horizontal planes at the depths z and $z + \Delta z$, is denoted with $B(z)$. All this together gives:

$$\frac{\partial}{\partial z} \lim_{\Delta z \to 0} \frac{1}{\Delta z} \int\limits_{V(z)} F_z(\vec{x},t)\,\mathrm{d}V =$$
$$\lim_{\Delta z \to 0} \frac{1}{\Delta z} \int\limits_{V(z)} \frac{\partial}{\partial z} F_z(\vec{x},t)\,\mathrm{d}V + \lim_{\Delta z \to 0} \frac{1}{\Delta z} \oint\limits_{B(z)} F_z(\vec{x},t)\vec{u}_A \cdot \vec{n}_A\,\mathrm{d}A\ . \tag{3.9}$$

By applying this formula to equation (3.7) following expression is obtained.

$$\begin{aligned}
A\frac{\partial\bar{\varphi}}{\partial t} = &\lim_{\Delta z\to 0}\frac{1}{\Delta z}\int\limits_{V(z)}\left\{\frac{\partial}{\partial x}\left(\kappa\frac{\partial\varphi}{\partial x}\right)+\frac{\partial}{\partial y}\left(\kappa\frac{\partial\varphi}{\partial y}\right)\right\}\mathrm{d}V+\\
&\frac{\partial}{\partial z}\lim_{\Delta z\to 0}\frac{1}{\Delta z}\int\limits_{V(z)}\kappa\frac{\partial\varphi}{\partial z}\,\mathrm{d}V-\lim_{\Delta z\to 0}\frac{1}{\Delta z}\oint\limits_{B(z)}\kappa\frac{\partial\varphi}{\partial z}\vec{u}_A\cdot\vec{n}_A\,\mathrm{d}A-\\
&\lim_{\Delta z\to 0}\frac{1}{\Delta z}\int\limits_{V(z)}\left\{\frac{\partial(u_x\varphi)}{\partial x}+\frac{\partial(u_y\varphi)}{\partial y}\right\}\mathrm{d}V-\\
&\frac{\partial}{\partial z}\lim_{\Delta z\to 0}\frac{1}{\Delta z}\int\limits_{V(z)}u_z\varphi\,\mathrm{d}V+\lim_{\Delta z\to 0}\frac{1}{\Delta z}\oint\limits_{B(z)}u_z\varphi\vec{u}_A\cdot\vec{n}_A\,\mathrm{d}A
\end{aligned}\tag{3.10}$$

The two integrals containing derivatives with respect to x and y can be examined by using Gauss' theorem

$$\int\limits_V\nabla\cdot\vec{F}\,\mathrm{d}^{(n)}x=\oint\limits_A\vec{F}\cdot\vec{n}\,\mathrm{d}^{(n-1)}x\;,\tag{3.11}$$

which is here used in an adapted way:

$$\int\limits_V\left\{\frac{\partial F_x}{\partial x}+\frac{\partial F_y}{\partial y}\right\}\mathrm{d}V=\oint\limits_A\left\{F_xn_x+F_yn_y\right\}\mathrm{d}A\;.\tag{3.12}$$

Utilising Gauss' theorem in this form results in

$$\begin{aligned}
A\frac{\partial\bar{\varphi}}{\partial t} = &\lim_{\Delta z\to 0}\frac{1}{\Delta z}\oint\limits_{B(z)}\left\{\kappa\frac{\partial\varphi}{\partial x}n_{A_x}+\kappa\frac{\partial\varphi}{\partial y}n_{A_y}\right\}\mathrm{d}A+\\
&\frac{\partial}{\partial z}\lim_{\Delta z\to 0}\frac{1}{\Delta z}\int\limits_{V(z)}\kappa\frac{\partial\varphi}{\partial z}\,\mathrm{d}V-\lim_{\Delta z\to 0}\frac{1}{\Delta z}\oint\limits_{B(z)}\kappa\frac{\partial\varphi}{\partial z}\vec{u}_A\cdot\vec{n}_A\,\mathrm{d}A-\\
&\lim_{\Delta z\to 0}\frac{1}{\Delta z}\oint\limits_{B(z)}\left\{u_x\varphi n_{A_x}+u_y\varphi n_{A_y}\right\}\mathrm{d}A-\\
&\frac{\partial}{\partial z}\lim_{\Delta z\to 0}\frac{1}{\Delta z}\int\limits_{V(z)}u_z\varphi\,\mathrm{d}V+\lim_{\Delta z\to 0}\frac{1}{\Delta z}\oint\limits_{B(z)}u_z\varphi\vec{u}_A\cdot\vec{n}_A\,\mathrm{d}A\;.
\end{aligned}$$

These integrals can be merged to

$$\begin{aligned}
A\frac{\partial\bar{\varphi}}{\partial t} = &\frac{\partial}{\partial z}\lim_{\Delta z\to 0}\frac{1}{\Delta z}\int\limits_{V(z)}\kappa\frac{\partial\varphi}{\partial z}\,\mathrm{d}V-\frac{\partial}{\partial z}\lim_{\Delta z\to 0}\frac{1}{\Delta z}\int\limits_{V(z)}u_z\varphi\,\mathrm{d}V+\\
&\lim_{\Delta z\to 0}\frac{1}{\Delta z}\oint\limits_{B(z)}\left\{\left(\kappa\frac{\partial\varphi}{\partial x}-u_x\varphi\right)n_{A_x}+\left(\kappa\frac{\partial\varphi}{\partial y}-u_y\varphi\right)n_{A_y}-\right.\\
&\left.\left(\kappa\frac{\partial\varphi}{\partial z}-u_z\varphi\right)\vec{u}_A\cdot\vec{n}_A\right\}\mathrm{d}A\;.
\end{aligned}\tag{3.13}$$

The three parentheses $F_i = \left(\kappa \frac{\partial \varphi}{\partial x_i} - u_i \varphi\right)$ are vector components of the total flux $\vec{F}$ composed of the diffusive and advective flux. The factors behind each of the parentheses are also components of a vector which will be named $\vec{n}$. In the following it will be shown that this vector $\vec{n}$ is normal to the boundary surface B. This geometry is visualised in figure 3.2. If it is assumed that this is true, then the terms inside the last integral in equation (3.13) can be expressed as $\vec{F} \cdot \vec{n}$, which is a quantity for the amount of tracer passing the boundary. In the case of a boundary which lets no tracer pass, it can be formulated as $\vec{F} \cdot \vec{n} = 0$.

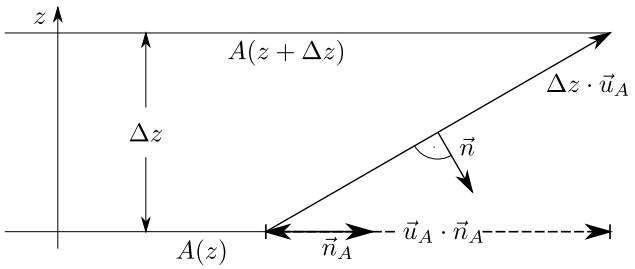

Figure 3.2: A slice of the geometry of the boundary of an arbitrary bathymetry.

At first the vectors involved in the proof that $\vec{n}$ is perpendicular to the boundary surface will be written down.

$$\begin{aligned}
\vec{n} &= n_{A_x}\vec{e}_x + n_{A_y}\vec{e}_y - \vec{u}_A \cdot \vec{n}_A \vec{e}_z \\
\vec{n}_A &= n_{A_x}\vec{e}_x + n_{A_y}\vec{e}_y + 0\vec{e}_z \\
\vec{u}_A &= \frac{\partial x}{\partial z}\vec{e}_x + \frac{\partial y}{\partial z}\vec{e}_y + \frac{\partial z}{\partial z}\vec{e}_z = \frac{\partial x}{\partial z}\vec{e}_x + \frac{\partial y}{\partial z}\vec{e}_y + 1\vec{e}_z = u_{A_x}\vec{e}_x + u_{A_y}\vec{e}_y + \vec{e}_z
\end{aligned}$$

The z-component of $\vec{n}_A$ is always zero because the vector lies in the plane perpendicular to the z-axis. When looking along the z-axis the vector $\vec{n}$ points in the same direction as the vector $\vec{n}_A$, which is obvious due to the same x- and y-components of these vectors. That means $\vec{n}$ lies in the plane defined by $\vec{n}_A$ and $\vec{u}_A$. To show that $\vec{n}$ is also perpendicular to $\vec{u}_A$ it is utilised that $\vec{x} \cdot \vec{y} = 0$ is only valid if $\vec{x}$ and $\vec{y}$ are perpendicular to each other:

$$\begin{aligned}
&\vec{u}_A \cdot \vec{n} = \\
&u_{A_x} n_x + u_{A_y} n_y + u_{A_z} n_z = \\
&u_{A_x} n_{A_x} + u_{A_y} n_{A_y} - \vec{u}_A \cdot \vec{n}_A = \\
&u_{A_x} n_{A_x} + u_{A_y} n_{A_y} + u_{A_z} n_{A_z} - \vec{u}_A \cdot \vec{n}_A = \\
&\vec{u}_A \cdot \vec{n}_A - \vec{u}_A \cdot \vec{n}_A = 0 \qquad \square
\end{aligned}$$

Now a new variable for a source coming from the basin boundary can be introduced

$$q(z) = \lim_{\Delta z \to 0} \frac{1}{B(z, \Delta z)} \oint\limits_{B(z,\Delta z)} \vec{F} \cdot \vec{n} \, \mathrm{d}A \, . \tag{3.14}$$

The variable q describes the amount of tracer of φ coming from "outside" the examined system and entering it at the depth z. It denotes the horizontally averaged source

which has the consequence that a source at only one point $p_{source} = p_{source}(x, y, z)$ on the boundary at depth z would enter the basin at depth z as an averaged source over the whole horizontal slice of the basin. The source has the dimension of $[q] = \mathrm{ms}^{-1}\,[\varphi]$. This source term does not appear in the three-dimensional transport equations, it is obtained by integrating equations (3.1) because a new boundary is introduced by this integration. If a source is to be included when using equations (3.1) to model a basin, then the model domain has to be expanded until a sensible geometrical constraint, e.g. a river mouth, where boundary conditions can be prescribed. The boundary surface can be approximated by $B \approx \Delta z \frac{\Delta A}{\Delta z}$. The greater $\frac{\Delta A}{\Delta z}$ the better the approximation. With this approximation and by applying the limit to $\frac{\Delta A}{\Delta z}$, equation (3.14) can be reformulated as

$$\frac{\mathrm{d}A}{\mathrm{d}z} q = \lim_{\Delta z \to 0} \frac{1}{\Delta z} \oint\limits_{B(z,\Delta z)} \vec{F} \cdot \vec{n}\, \mathrm{d}A\,.$$

With this result, equation (3.13) becomes

$$A \frac{\partial \bar{\varphi}}{\partial t} = \frac{\partial}{\partial z} \lim_{\Delta z \to 0} \frac{1}{\Delta z} \int\limits_{V(z)} \kappa \frac{\partial \varphi}{\partial z}\, \mathrm{d}V - \frac{\partial}{\partial z} \lim_{\Delta z \to 0} \frac{1}{\Delta z} \int\limits_{V(z)} u_z \varphi\, \mathrm{d}V + \frac{\mathrm{d}A}{\mathrm{d}z} q\,. \tag{3.15}$$

In order to calculate these remaining two integrals, a decomposition of the variables φ, κ, and u_z is made in analogy to the Reynolds decomposition. But instead of using an ensemble average, a spatial average over the horizontal area of the hypsographical function A is applied. Such an average was already introduced with equation (3.5). Because the variable $\bar{\varphi}$ is an average over a horizontal volume slice of the basin, it does not depend on the horizontal coordinates. The fluctuating part of the decomposition is, in analogy to the Reynolds decomposition, defined by $\tilde{\varphi}(\vec{x}, t) := \varphi(\vec{x}, t) - \bar{\varphi}(z, t)$. By applying this decomposition to the three variables φ, κ and u_z, they can be written as

$$\begin{aligned}
\varphi(\vec{x}, t) &= \lim_{\Delta z \to 0} \frac{1}{\Delta z A(z)} \int\limits_{V(z)} \varphi(\vec{x}, t)\, \mathrm{d}V + \tilde{\varphi}(\vec{x}, t) = \bar{\varphi}(z, t) + \tilde{\varphi}(\vec{x}, t) \\
\kappa(\vec{x}, t) &= \lim_{\Delta z \to 0} \frac{1}{\Delta z A(z)} \int\limits_{V(z)} \kappa(\vec{x}, t)\, \mathrm{d}V + \tilde{\kappa}(\vec{x}, t) = \bar{\kappa}(z, t) + \tilde{\kappa}(\vec{x}, t) \\
u_z(\vec{x}, t) &= \lim_{\Delta z \to 0} \frac{1}{\Delta z A(z)} \int\limits_{V(z)} u_z(\vec{x}, t)\, \mathrm{d}V + \tilde{u}_z(\vec{x}, t) = \bar{u}_z(z, t) + \tilde{u}_z(\vec{x}, t)\,.
\end{aligned}$$

Inserting the decomposed variables into equation (3.15) results in

$$\begin{aligned}
A \frac{\partial \bar{\varphi}}{\partial t} = \frac{\partial}{\partial z} \lim_{\Delta z \to 0} \frac{1}{\Delta z} \int\limits_{V(z)} \Big(\bar{\kappa} \frac{\partial \bar{\varphi}}{\partial z} + \tilde{\kappa} \frac{\partial \tilde{\varphi}}{\partial z} + \underbrace{\bar{\kappa} \frac{\partial \tilde{\varphi}}{\partial z}}_{=0} + \underbrace{\tilde{\kappa} \frac{\partial \bar{\varphi}}{\partial z}}_{=0} \Big)\, \mathrm{d}V - \\
\frac{\partial}{\partial z} \lim_{\Delta z \to 0} \frac{1}{\Delta z} \int\limits_{V(z)} (\bar{u}_z \bar{\varphi} + \tilde{u}_z \tilde{\varphi} + \underbrace{\bar{u}_z \tilde{\varphi}}_{=0} + \underbrace{\tilde{u}_z \bar{\varphi}}_{=0})\, \mathrm{d}V + \frac{\mathrm{d}A}{\mathrm{d}z} q\,.
\end{aligned}$$

The terms containing a mixed product of a fluctuating and an averaged variable vanish, because the integral being applied to them is nothing else as the spatial average used

for the decomposition and the fluctuating quantities are zero in average (see the Reynolds rules in chapter 2.1.3). The underbraces indicating that the individual terms vanish should therefore not be misunderstood as they only vanish if the integral is applied. The terms containing a product of two averaged variables do not depend on the horizontal coordinates x or y anymore so the integrals can easily be calculated. With the terms containing the product of two fluctuating variables still to be evaluated, this yields

$$A\frac{\partial\bar{\varphi}}{\partial t} = \frac{\partial}{\partial z}\left(A\bar{\kappa}\frac{\partial\bar{\varphi}}{\partial z}\right) - \frac{\partial}{\partial z}(A\bar{u}_z\bar{\varphi}) + \lim_{\Delta z\to 0}\frac{1}{\Delta z}\int\limits_{V(z)}\left(\tilde{\kappa}\frac{\partial\tilde{\varphi}}{\partial z} - \tilde{u}_z\tilde{\varphi}\right)\mathrm{d}V + \frac{\mathrm{d}A}{\mathrm{d}z}q\ .$$

If it is assumed that the quantities $\tilde{\kappa}$ and $\tilde{\varphi}$ and the quantities $\tilde{u}_z$ and $\tilde{\varphi}$ are not correlated in any way, then this integral becomes zero too, because the average of the product of two fluctuating quantities $\langle x'y'\rangle$ is the correlation of these two quantities. Now the variables $\bar{\varphi}$, $\bar{\kappa}$, and $\bar{u}_z$ can be renamed to φ, κ, and w which finally results in the final equation

$$\frac{\partial\varphi}{\partial t} = \frac{1}{A}\frac{\partial}{\partial z}\left(A\kappa\frac{\partial\varphi}{\partial z}\right) - \frac{1}{A}\frac{\partial}{\partial z}(Aw\varphi) + \frac{1}{A}\frac{\mathrm{d}A}{\mathrm{d}z}q\ . \tag{3.16}$$

This equation can be transformed, so that it consists of a true diffusive and a true advective part. This transformation can be done by applying the product rule inside the first derivative with respect to z and by multiplying one term with A/A.

$$\begin{aligned}
\frac{\partial(A\varphi)}{\partial t} &= \frac{\partial}{\partial z}\left(A\kappa\frac{\partial\varphi}{\partial z}\right) - \frac{\partial}{\partial z}\left(Aw\varphi\right) + \frac{\mathrm{d}A}{\mathrm{d}z}q \\
\frac{\partial(A\varphi)}{\partial t} &= \frac{\partial}{\partial z}\left(\kappa\frac{\partial(A\varphi)}{\partial z}\right) - \frac{\partial}{\partial z}\left(\frac{\mathrm{d}A}{\mathrm{d}z}\frac{\kappa}{A}(A\varphi)\right) - \frac{\partial}{\partial z}\left(w(A\varphi)\right) + \frac{\mathrm{d}A}{\mathrm{d}z}q \\
\frac{\partial\phi}{\partial t} &= \frac{\partial}{\partial z}\left(\kappa\frac{\partial\phi}{\partial z}\right) - \frac{\partial}{\partial z}\left(\left\{\frac{\mathrm{d}A}{\mathrm{d}z}\frac{\kappa}{A} + w\right\}\phi\right) + \frac{\mathrm{d}A}{\mathrm{d}z}q
\end{aligned} \tag{3.17}$$

Equation (3.17) is valid for the new variable $\phi = A\varphi$. The advection speed is $w_d = \frac{\mathrm{d}A}{\mathrm{d}z}\frac{\kappa}{A} + w$. This form of the equation only consists of flux terms and one source term which means that, if the source term vanishes, it has the form of a conservation law. This again means that, even in a discretised form and using a finite volume scheme, the equation is conservative and no artificial sinks or sources due to numerical errors can appear. However, later it will be shown that equation (3.16) is also conservative in a discretised form. The big advantage of equation (3.17) for ϕ is that it can be easily integrated into already existing models as the numerical diffusion and advection routines do not have to be modified. The results of this approach are discussed in section 4.2.
The derivation of the one-dimensional momentum equation from the three-dimensional equations

$$\frac{\partial u_i}{\partial t} + u_j\frac{\partial u_i}{\partial x_j} = \frac{\partial}{\partial x_j}\left(\nu\frac{\partial u_i}{\partial x_j}\right)\ , \tag{3.18}$$

with $i = x, y, z$, can be done in analogy to the derivation of the tracer equation 3.16. The resulting equations are

$$\frac{\partial\bar{u}_i}{\partial t} + \frac{1}{A}\frac{\partial}{\partial z}(A\bar{u}_z\bar{u}_i) = \frac{1}{A}\frac{\partial}{\partial z}\left(A\bar{\nu}\frac{\partial\bar{u}_i}{\partial z}\right) + \frac{1}{A}\frac{\mathrm{d}A}{\mathrm{d}z}f_i\ , \tag{3.19}$$

where the index is now $i = x, y$. In this case the source f can be identified with the friction caused by the water flowing along the basin boundary. Thus, it is a sink of momentum and is parameterised in the usual way (see e.g. *Kundu and Cohen* (2008)):

$$f_i = -c_D \bar{u}_i \sqrt{\bar{u}_x^2 + \bar{u}_y^2} \, . \tag{3.20}$$

With this parameterisation, the final one-dimensional momentum equations are

$$\frac{\partial \bar{u}_i}{\partial t} + \frac{1}{A}\frac{\partial}{\partial z}(A \bar{u}_z \bar{u}_i) = \frac{1}{A}\frac{\partial}{\partial z}\left(A \bar{\nu} \frac{\partial \bar{u}_i}{\partial z}\right) - \frac{1}{A}\frac{\mathrm{d}A}{\mathrm{d}z} c_D \bar{u}_i \sqrt{\bar{u}_x^2 + \bar{u}_y^2} \, . \tag{3.21}$$

3.2 Deriving an analytical solution

An analytical solution will be derived for the modified diffusion equation

$$\frac{\partial \varphi}{\partial t} = \frac{1}{A}\frac{\partial}{\partial z}\left(A \kappa \frac{\partial \varphi}{\partial z}\right) \, , \tag{3.22}$$

which includes the hypsography and which was derived in section 3.1. For the initial condition and the boundary conditions it is assumed that

$$\varphi(z, t = 0) = \varphi_0 \delta(z - z_0) \tag{3.23}$$

$$\varphi(z = \pm\infty, t) = 0 \, , \tag{3.24}$$

with δ being the Dirac delta distribution.
The hypsographical function is chosen to be $A(z) = A_0 \, \mathrm{e}^{n(z+H)}$ with A_0 being the area of the basin at the depth H and n being an arbitrary factor with the dimension of an inverse length.
For the derivation of the solution, the Fourier transform

$$\varphi = \frac{1}{2\pi} \int_{-\infty}^{\infty} \mathrm{d}k \, \hat{\varphi} \, \mathrm{e}^{ikz}$$

$$\hat{\varphi} = \int_{-\infty}^{\infty} \mathrm{d}z \, \varphi \, \mathrm{e}^{-ikz}$$

will be used. The modified diffusion equation (3.22) can be written as

$$\frac{\partial \varphi}{\partial t} - \kappa \frac{\frac{\mathrm{d}A}{\mathrm{d}z}}{A}\frac{\partial \varphi}{\partial z} - \kappa \frac{\partial^2 \varphi}{\partial z^2} = 0 \, .$$

With $\frac{\frac{\mathrm{d}A}{\mathrm{d}z}}{A} = n$ it simplifies to

$$\frac{\partial \varphi}{\partial t} - \kappa n \frac{\partial \varphi}{\partial z} - \kappa \frac{\partial^2 \varphi}{\partial z^2} = 0 \, .$$

Now φ can be substituted by its Fourier transform and it can be differentiated under the integral sign:

$$\frac{1}{2\pi}\int_{-\infty}^{\infty}\mathrm{d}k\left\{\frac{\partial}{\partial t}\hat{\varphi}\,\mathrm{e}^{ikz}-\kappa n\frac{\partial}{\partial z}\hat{\varphi}\,\mathrm{e}^{ikz}-\kappa\frac{\partial^2}{\partial z^2}\hat{\varphi}\,\mathrm{e}^{ikz}\right\}=0$$
$$\frac{1}{2\pi}\int_{-\infty}^{\infty}\mathrm{d}k\,\mathrm{e}^{ikz}\left\{\frac{\partial\hat{\varphi}}{\partial t}-i\kappa nk\hat{\varphi}+\kappa k^2\hat{\varphi}\right\}=0\,.$$

This equation can only be fulfilled, if the equation

$$\frac{\partial\hat{\varphi}}{\partial t}-i\kappa nk\hat{\varphi}+\kappa k^2\hat{\varphi}=0$$

is satisfied. This is a first order ordinary differential equation for $\hat{\varphi}$. It can be solved by separating the variables:

$$\int\frac{\mathrm{d}\hat{\varphi}}{\hat{\varphi}}=\int\mathrm{d}t\left\{i\kappa nk-\kappa k^2\right\}$$
$$\hat{\varphi}=\hat{\varphi}_0\,\mathrm{e}^{\kappa t(ink-k^2)}\,.$$

The constant of integration can be determined be transforming the initial condition into Fourier space:

$$\hat{\varphi_0}=\hat{\varphi}(z,t=0)=\varphi_0\int_{-\infty}^{\infty}\mathrm{d}z\delta(z-z_0)\,\mathrm{e}^{-ikz}=\varphi_0\,\mathrm{e}^{-ikz_0}\,.$$

This yields a unique solution in the Fourier space:

$$\hat{\varphi}=\varphi_0\exp\left\{-\kappa tk^2+i\kappa tk\left(n-\frac{z_0}{\kappa t}\right)\right\}$$

With this solution, the transformation back into the time domain can be done.

$$\varphi=\frac{\varphi_0}{2\pi}\int_{-\infty}^{\infty}\mathrm{d}k\exp\left\{-\kappa tk^2+i\kappa tk\left(n-\frac{z_0}{\kappa t}\right)+ikz\right\}$$
$$\varphi=\frac{\varphi_0}{2\pi}\int_{-\infty}^{\infty}\mathrm{d}k\exp\left\{-\kappa t\left[k^2-ik\left(n+\frac{z-z_0}{\kappa t}\right)\right]\right\}$$

By completing the square of the argument of the exponential function the integral can be solved by substitution.

$$\varphi = \frac{\varphi_0}{2\pi} \int_{-\infty}^{\infty} \mathrm{d}k \exp\left\{-\kappa t \left[\left(k - \frac{i}{2}\left(n + \frac{z - z_0}{\kappa t}\right)\right)^2 - \frac{1}{4}\left(n + \frac{z - z_0}{\kappa t}\right)^2\right]\right\}$$

$$\varphi = \frac{\varphi_0}{2\pi} \exp\left\{-\frac{\kappa t}{4}\left(n + \frac{z - z_0}{\kappa t}\right)^2\right\} \int_{-\infty}^{\infty} \mathrm{d}k \exp\left\{-\kappa t \underbrace{\left[k - \frac{i}{2}\left(n + \frac{z - z_0}{\kappa t}\right)\right]^2}_{=\chi}\right\}$$

$$\varphi = \frac{\varphi_0}{\pi} \exp\left\{-\frac{\kappa t}{4}\left(n + \frac{z - z_0}{\kappa t}\right)^2\right\} \int_{0}^{\infty} \mathrm{d}\chi \, \mathrm{e}^{-\kappa t \chi^2}$$

The integral is solved by

$$\int_0^{\infty} \mathrm{d}\chi \, \mathrm{e}^{-\kappa t \chi^2} = \frac{1}{2}\sqrt{\frac{\pi}{\kappa t}} \,, \tag{3.25}$$

(*Bronstein and Semendjajew*, 2005) which yields the final solution

$$\varphi(z,t) = \frac{\varphi_0}{\sqrt{4\pi\kappa t}} \exp\left\{-\frac{\kappa t}{4}\left(n + \frac{z - z_0}{\kappa t}\right)^2\right\} \,. \tag{3.26}$$

This solution can be compared to the well-known analytical solution for the original diffusion equation:

$$\varphi(z,t) = \frac{\varphi_0}{\sqrt{4\pi\kappa t}} \exp\left\{-\frac{(z - z_0)^2}{4\kappa t}\right\} \,. \tag{3.27}$$

Equation (3.26) is equal to equation (3.27) if and only if $n = 0$ implying $A = A_0$. This result can be interpreted as the absence of any boundaries which is identical to the assumption of a horizontally infinite ocean. Exactly this situation is assumed when formulating the original one-dimensional diffusion equation. Thus, it can be said that the new solution is consistent with the old one.

The constant n has the consequence that the Gaussian function gets shifted into the direction in which the hypsographical function decreases. This shift can be explained by looking at the total mass of the tracer φ needed to reach a certain concentration. If the hypsography is large, then a large amount of the tracer is needed to reach a certain concentration because the dilution is greater. Thus, a higher concentration is reached faster in regions with a small hypsography and, in this case, the Gaussian function of the concentration grows faster where the hypsography is smaller which happens to be further down in the water column. This dynamic explains the downward shift of the concentration. Figure 3.3 shows the graphs of equations (3.26) and (3.27) with the same initial conditions and after the same period of time.

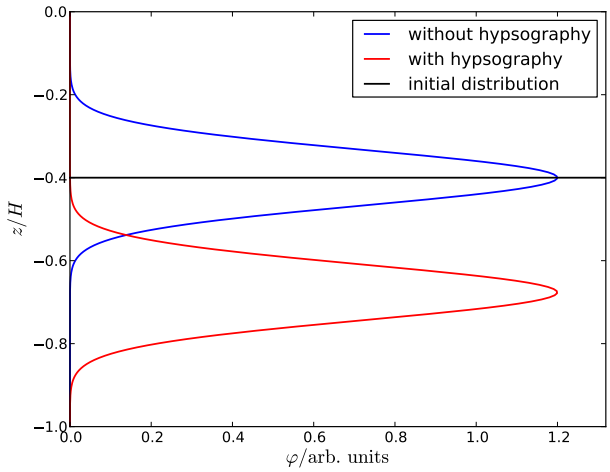

Figure 3.3: The influence of the hypsography on the analytical solution of the modified diffusion equation.

3.3 The entrainment model

A simple entrainment model for calculating the effects of entrainment on the dense bottom current moving from the Arcona Basin to the Gotland Basin will be derived here. This model is based upon the work of *Stigebrandt* (1987). The derivation will start with a momentum equation which includes frictional forces and longitudinal pressure gradient forces

$$\frac{\partial u}{\partial t} - \frac{\partial}{\partial z}\left(\nu \frac{\partial u}{\partial z}\right) = -\frac{1}{\rho}\frac{\partial p}{\partial x} \,, \tag{3.28}$$

with u being the velocity, ν the eddy diffusivity for momentum, ρ the density and p denotes the pressure. The boundary conditions are

$$\nu \frac{\partial u}{\partial z} = \frac{\tau_s}{\rho} \quad \text{for } z = 0 \tag{3.29}$$

$$\nu \frac{\partial u}{\partial z} = \frac{\tau_b}{\rho} \quad \text{for } z = -H \,, \tag{3.30}$$

where τ_s and τ_b are the frictional stresses at the surface and the bottom, respectively. Equation (3.28) will be applied to following scenario. It is assumed that two basins are connected by a channel of constant width B with a slope of s. A lighter fluid sits on top of a denser fluid and the water level of the denser water is higher in the left basin than in the right one and thus flows from the left to the right basin. The height of the denser fluid in the channel is h and the density, the salinity and the temperature of the denser fluid are denoted with ρ_d, S_d, and T_d, respectively. The lighter fluid acts as a thermal and saline reservoir with ρ_a, S_d, and T_d being the ambient density, salinity, and temperature, respectively. Figure 3.4 shows the channel flow together with some variables important for this derivation. Because of the simple geometry, $\mathrm{d}p = \rho g' \mathrm{d}z$ and $\frac{\mathrm{d}z}{\mathrm{d}x} = s$ can be utilised to express the right hand side of equation (3.28) giving

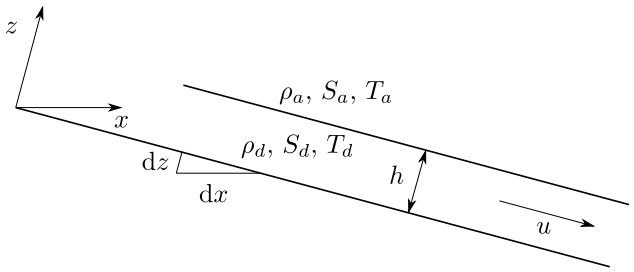

Figure 3.4: The geometrical setup for the entrainment model with the slope being $s = \frac{\mathrm{d}z}{\mathrm{d}x}$ (after *Stigebrandt* (1987)).

$$-\frac{1}{\rho}\frac{\partial p}{\partial x} = -\frac{1}{\rho}\frac{\partial p}{\partial z}\frac{\mathrm{d}z}{\mathrm{d}x} = -g's$$

for the longitudinal pressure gradient force, with $g' = g\Delta\rho/\rho$ being the buoyancy. If a steady flow is governed by balancing the two forces, the time derivative $\frac{\partial u}{\partial t}$ vanishes and an integration over the whole denser part of the water column can be applied. Together with the boundary conditions this yields

$$-\frac{\tau_s}{\rho} + \frac{\tau_b}{\rho} = -g'hs \; . \tag{3.31}$$

The left hand side describes the frictional stresses at the bottom and at the interface between the two fluids. This can be parameterised by using a combined drag coefficient C_d for the bottom and surface stresses.

$$C_d u^2 = g'hs \; . \tag{3.32}$$

Thus, the flow velocity is

$$u = \sqrt{g'hs/C_d} \; . \tag{3.33}$$

Because the flow is unidirectional, a case-by-case analysis for the sign is needless when extracting the root. If the volume flow Q is considered as an independent variable, it is determined by $Q = uBh$. The specific volume flow $q = Q/B = uh$ can be used to substitute h in equation (3.33):

$$u = \sqrt[3]{qg's/C_d} \; . \tag{3.34}$$

The friction velocity is defined as $u_*^2 = C_d u^2$, which is needed for the entrainment model introduced by *Kato and Phillips* (1969). In this case, the entrainment velocity is

$$w_e = \frac{2m_0 u_*^3}{g'h} = 2m_0\sqrt{C_d}su$$

with m_0 being an empirical constant. The entrainment velocity w_e expresses the increase of the specific volume flow along the channel:

$$\frac{\mathrm{d}q}{\mathrm{d}x} = w_e \; ,$$

which means that the increase of the specific volume flow $\frac{\mathrm{d}q}{\mathrm{d}x}$ can be expressed by the three constants m_0, C_d, and s and by the flow speed u:

$$\mathrm{d}q = 2m_0 su\sqrt{C_d}\mathrm{d}x \ . \tag{3.35}$$

With this equation the volume flow flowing into the right basin can be calculated. The entrainment influences the salinity S_d and the temperature T_d of the dense current by gradually converging these properties to the salinity S_a and temperature T_a of the upper lighter fluid:

$$\mathrm{d}S_d = (S_a - S_d)\frac{\mathrm{d}q}{q + \mathrm{d}q} \tag{3.36}$$

$$\mathrm{d}T_d = (T_a - T_d)\frac{\mathrm{d}q}{q + \mathrm{d}q} \tag{3.37}$$

The three equations (3.35), (3.36) and (3.37) can be calculated in an iteratively manner. When the distance $\mathrm{d}x$ between the two basins is reached, an inflow occurs in the right basin. But if the density difference $\Delta\rho = \rho_a - \rho_d$ vanishes, the dense current is completely diluted and will not reach the basin. The density is calculated by means of the EOS80, the UNESCO equation of state from 1983 (*Fofonoff and Millard*, 1983).
Following configuration for the parameters was used to calculate the effects of entrainment. The distance between the Arcona Basin and the Gotland Basin was assumed to be 640 km (*Feistel et al.*, 2008) with the dense bottom current needing 3 months to reach the Gotland Basin (*Reissmann et al.*, 2009). The "slope" of the Baltic Sea between the Arcona Basin and the Gotland Basin was calculated by taking the depth difference between the two basins and dividing it by the distance between them which results in a slope of $s = 10^{-4}$. The constant width of the bottom current was calculated by an optimising algorithm which varied the width to fit the highest measured bottom salinity in the Gotland Basin, the result was $B = 30\,\mathrm{km}$, which is in good agreement with the width calculated by *Stigebrandt* (1987). The combined drag coefficient of the bottom friction and the interface friction between the two fluids was assumed to be $C_d = 3 \cdot 10^{-3}$. The value for the empirical constant m_0 was taken from *Stigebrandt* (1985) which is $m_0 = 0.6$. The ambient salinity of the Baltic Proper was assumed to be $S_a = 10\,\mathrm{g/kg}$ and the temperature of $8\,^\circ\mathrm{C}$ was varied with a sine function with an amplitude of $3\,^\circ\mathrm{C}$ and a cycle of one year according to *Stigebrandt* (1987).

3.4 Including inflows

For modelling inflows, the source term in equation (3.16) is used. As a reminder, the variable q was approximated with

$$q = \left(\frac{\mathrm{d}A}{\mathrm{d}z}\right)^{-1} \lim_{\Delta z \to 0} \frac{1}{\Delta z} \oint\limits_{B(z,\Delta z)} \vec{F} \cdot \vec{n}\, \mathrm{d}A \ .$$

The total flux of a tracer φ into the basin is equation (3.14) integrated over the whole water depth which is

$$Q_\varphi = \int\limits_{-H}^{0} \mathrm{d}z \lim_{\Delta z \to 0} \frac{1}{\Delta z} \oint\limits_{B(z,\Delta z)} \vec{F} \cdot \vec{n}\, \mathrm{d}A \ . \tag{3.38}$$

If the approximated source q is inserted into equation (3.38), following relationship between q and Q_φ can be found

$$\int_{-H}^{0} \mathrm{d}z \, \frac{\mathrm{d}A}{\mathrm{d}z} q = Q_\varphi \ , \tag{3.39}$$

with

$$Q_\varphi = \varphi_I Q_I \tag{3.40}$$

and Q_I being the volume transport of water and φ_I being the concentration of the imported tracer. This transport is related to the total water volume V_I of an inflow which gets transported into a basin by following relationship. If an inflow starts at $t = t_1$ and ends at $t = t_2$ following expression can be formulated

$$V_I = \int_{t_1}^{t_2} \mathrm{d}t \, Q_I \ .$$

If the properties of the inflowing water are only known somewhere far away from the modelled basin (e.g. like in this thesis where the Gotland Basin is modelled and the data for the inflows is taken from a transect across the Arcona basin) the entrainment model derived in section 3.3 can be utilised. The volume flow Q_I can be calculated by using equation (3.35). The salinity and temperature of the inflowing dense current may be obtained by equations (3.36) and (3.37), respectively. After the current arrives at the basin, it interleaves at a depth where the residing water has the same density as the inflowing water. The newly arrived water masses push the masses of water above them upwards, which is a consequence of mass conservation. The vertical advection velocity is

$$w = Q_I / A \ . \tag{3.41}$$

The water reaching the upper layers of the water column eventually end up as a more or less brackish outflow. This outflow in the upper layers of the water column balances all the inflows happening in the deeper parts.

3.5 The scope of application

Before running a one-dimensional model it should be ensured that it is justified to restrict the dynamics to one dimension. This means that horizontal gradients have to be far smaller than vertical gradients. There are several origins of forces that could break this assumption. These could be the atmospheric forcing, in- and outflows, the Coriolis force, or differential heating. Differential heating could be caused by shallow regions where the water heats up or cools down more quickly. It has to be assumed that the horizontal variations of the atmospheric forcing are small enough to be represented by observations only made at one place and that effects like convective overturning due to the sinking of cooled surface water are homogeneous enough.
The effects of the in- and outflows on the one-dimensional structure of the water in a basin can be evaluated by two different internal Froude numbers for inflows and outflows, respectively (*Patterson et al.*, 1984). These internal Froude numbers express the ratio of

inertial forces, excited by the inflows or outflows, to the pressure gradient forces induced by horizontal density gradients. The internal Froude number for inflows is defined as

$$F_I = \frac{u}{\sqrt{g'H}} \,, \tag{3.42}$$

with u being the velocity of the inflowing water, H being the total depth of the basin and g' being the buoyancy based upon the difference between the inflowing water density and the surface density of the basin. Values of $F_I < 1$ indicate that the pressure gradient forces affect the horizontal gradients faster than the inflows generate them which, in the end, means that the assumption of one-dimensionality is justified with respect to inflows. The internal Froude number for outflows is defined as

$$F_O = \frac{Q_{out}}{H^2\sqrt{g'H}} \,. \tag{3.43}$$

Here, Q_{out} denotes the outflowing water transport. A value of $F_O < 1$ also means that the horizontal gradients are small compared to vertical gradients.
The Coriolis force can cause effects like up- and downwelling or coastally trapped Kelvin waves which in turn destroy the assumptions made for a one-dimensional model. The influence of the Coriolis force can be evaluated by the internal Rossby radius defined as

$$R_I = \frac{\sqrt{g'h}}{f} \,, \tag{3.44}$$

where $f = 2\Omega \sin\Phi$ is the Coriolis parameter (Φ is the latitude), with $\Omega = \frac{2\pi}{86164\,\mathrm{s}}$ being the rotation period of the Earth. The internal Rossby radius is the length over which the Coriolis force balances pressure gradient forces generated by tilted interfaces. The ratio of the internal Rossby radius and the width of the basin B

$$R = \frac{R_I}{B} \tag{3.45}$$

is a measure for the impact of the Coriolis force. If $R > 1$, then the Coriolis force is small compared to the pressure gradient forces and the fluid dynamics can be described by a one-dimensional model.

3.6 Discretisation of the transport equations

For the calculation of the diffusion equation

$$\frac{\partial\varphi}{\partial t} - \frac{1}{A}\frac{\partial}{\partial z}\left(A\kappa\frac{\partial\varphi}{\partial z}\right) = 0$$

the model uses a semi-implicit central difference scheme:

$$\frac{\varphi_j^{n+1} - \varphi_j^n}{\Delta t} - \frac{A_{f_j}\kappa_j^n \frac{\varphi_{j+1}^{n+\sigma} - \varphi_j^{n+\sigma}}{\frac{1}{2}\left(h_{j+1}^{n+1} + h_j^{n+1}\right)} - A_{f_{j-1}}\kappa_{j-1}^n \frac{\varphi_j^{n+\sigma} - \varphi_{j-1}^{n+\sigma}}{\frac{1}{2}\left(h_j^{n+1} + h_{j-1}^{n+1}\right)}}{A_{c_j} h_j^{n+1}} = 0 \,. \tag{3.46}$$

$\varphi^{n+\sigma}$ is defined as $\varphi^{n+\sigma} := \sigma\varphi^{n+1} + (1-\sigma)\varphi^n$, with σ being a parameter determining how implicit the scheme is. For $\sigma = 0$ the scheme is fully explicit and for $\sigma = 1$ it is fully implicit. A_c is the hypsography at the grid centres and A_f is the hypsography at the grid

interfaces (see figure 2.1).
The advection equation

$$\frac{\partial \varphi}{\partial t} + \frac{1}{A}\frac{\partial}{\partial z}\left(Aw\varphi\right) = 0$$

is discretised by a simple first order upstream scheme:

$$\frac{\varphi_j^{n+1} - \varphi_j^n}{\Delta t} + \frac{A_{f_j} w_j^n \varphi_j^n - A_{f_{j-1}} w_{j-1}^n \varphi_{j-1}^n}{A_{c_j} h_j^{n+1}} = 0 \; . \tag{3.47}$$

These two schemes are applied successively in a scheme split technique for more generality with respect to the implementation of the model. This way they can be applied independently from each other.
In order to show the conservative nature of these two schemes, a new variable is introduced:

$$F_j^{n+\sigma} = A_{f_j} \kappa_j^n \frac{\varphi_{j+1}^{n+\sigma} - \varphi_j^{n+\sigma}}{\frac{1}{2}\left(h_{j+1}^{n+1} + h_j^{n+1}\right)} - A_{f_j} w_j^n \varphi_j^n \; , \tag{3.48}$$

which is the discretised advective and diffusive flux. Using this variable, the schemes can be combined and written as

$$\frac{\varphi_j^{n+1} - \varphi_j^n}{\Delta t} - \frac{F_j^{n+\sigma} - F_{j-1}^{n+\sigma}}{A_{c_j} h_j^{n+1}} = 0 \; . \tag{3.49}$$

The total amount of φ in the whole basin can be expressed as

$$M^n = \sum_{j=1}^{N} \varphi_j^n A_{c_j} h_j \; . \tag{3.50}$$

Here, φ_j^n gets multiplied with each discrete basin sub-volume $V_j = A_{c_j} h_j$. In order to show the conservative nature of this discretisation, the discretised time derivative of M^n has to be examined.

$$\begin{aligned} \frac{M^{n+1} - M^n}{\Delta t} &= \frac{\sum_{j=1}^{N} \varphi_j^{n+1} A_{c_j} h_j - \sum_{j=1}^{N} \varphi_j^n A_{c_j} h_j}{\Delta t} \\ \frac{M^{n+1} - M^n}{\Delta t} &= \sum_{j=1}^{N} \frac{\varphi_j^{n+1} - \varphi_j^{n+1}}{\Delta t} A_{c_j} h_j \end{aligned} \tag{3.51}$$

Inserting the discretisation (3.49) into equation (3.51) results in

$$\frac{M^{n+1} - M^n}{\Delta t} = \sum_{j=1}^{N} \left(F_j^{n+\sigma} - F_{j-1}^{n+\sigma}\right) \; .$$

When applying the sum, the two terms $F_j^{n+\sigma}$ and $F_{j-1}^{n+\sigma}$ cancel each other out for every index except for $j = 1$ and $j = N$:

$$\frac{M^{n+1} - M^n}{\Delta t} = F_N^{n+\sigma} - F_1^{n+\sigma} \; ,$$

with $F_N^{n+\sigma}$ and $F_1^{n+\sigma}$ being the surface flux and the bottom flux, respectively. This means that if no external fluxes through the surface or the bottom occur, then the total amount of $\tilde{\varphi}$ is conserved even in a numerically discretised form. This behaviour is often of great importance, if e.g. one is interested in the total amount of salt in a basin after a simulation period of several decades.
Everything in this section can be applied analogous to the momentum equations which gives the same results and discretised equations.

3.7 Implementation details of the model

The modifications and extensions done to the source code of GOTM can be separated into two different issues. The first major change in the code was done to incorporate the horizontally averaged dynamic equations and the effects introduced by these new equations. The hypsography has to be included for the calculation of the new equations. As a consequence, e.g. the friction has to be calculated at every grid point, which acts as a sink in the momentum equations. The second major change was done to calculate inflows. These are handled separately which means that they can be switched off explicitly in order to simulate basins without any kind of inflow.
Before entering the main time loop of the simulation, the hypsography gets initialised. The values are interpolated to the grid used by GOTM which means that the hypsography can be given at any arbitrary depth intervals. After this one initial step, the hypsography is updated once a time step and gets adapted to the possibly changed grid. This can happen, if for example σ-coordinates are used. Apart from providing the actual hypsographical function, the advection and diffusion routines needed to be modified to correctly discretise equation (3.16). This was done as shown in section 3.6. If the standard water column model is wished to be used, the hypsography is set to unity which results in the original advection and diffusion equations.
The entrainment of inflows prescribed far upstream is calculated offline by a separate routine. The results of this computation are saved as the actual inflows and are passed on to GOTM. The inflows are initialised before the main time loop starts. Values like the volume flow, the salinity and the temperature are interpolated both, to the appropriate time axis and to the depth axis. This also happens during the time loop every time new values are read in from file. The frequency of the reading in of new values depends on the time resolution with which they are provided to the model. If the water transport, which was read in from file, is greater than zero, the inflow algorithm starts. In order to find the interleaving depth of the inflowing water, the densities of the two water masses are compared at every grid cell. If they are equal, the interleaving depth is found. Should the volume of the inflowing water be so big that it does not fit into the volume of one grid cell $V_\mathrm{j} = A_{c_j} h_j$ the "inflow height" increases successively until it is large enough. From this information, the hypsography, and the inflow related values, read in from file, the source terms for salinity and temperature can be calculated. Subsequently the vertical flux is determined by adding up the whole water volume flowing into the basin below the current grid cell $F_{Q_j} = \sum_{i=1}^{j} Q_i$. From this, the vertical advection velocity can easily be calculated with $w_j = F_{Q_j}/A_{c_j}$ which gets passed on to the advection routine. Finally the sink terms due to the outflowing brackish water at the sea surface are computed by balancing the amount of inflowing water. Additionally, there is the possibility to include a water inflow

at the sea surface to incorporate, e.g. the river runoff which would be a fresh water inflow.

Chapter 4

Results

4.1 Idealised test cases

4.1.1 Comparison with an analytical solution

It is impossible to verify or validate a numerical model of natural systems (*Oreskes et al.*, 1994). But a numerical model must at least reproduce an analytical solution, if one is known. A convergence between the numerical and the analytical solution does not validate a model, because it only validates the numerical model in one certain point in the parameter space. And the reason why numerical models are used is to go beyond the initial conditions and the assumptions made for analytical solutions.

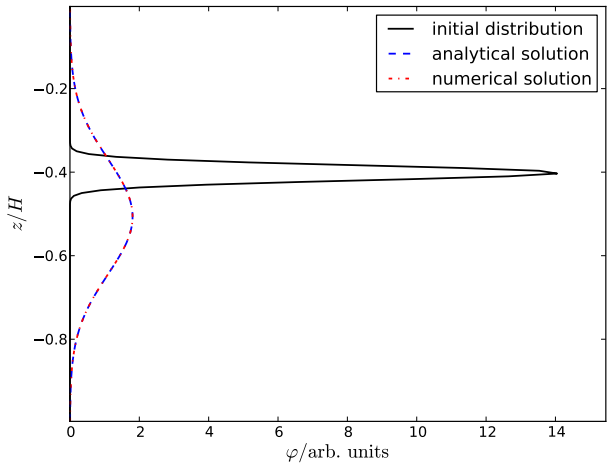

Figure 4.1: Comparison of the analytical solution (3.26) with the numerical solution.

In order to compare the numerical model with the analytical solution presented in section 3.2, the assumptions made for this solution have to be adopted by the model. A constant diffusivity is easily set up in the extended GOTM. The assumption that the solution vanishes at $\varphi(z = \pm\infty, t) = 0$ cannot be fulfilled by a numerical model like GOTM. But because the analytical solution is quadratically integrable $\left(\int_{-\infty}^{\infty} |\varphi(z)|^2 \, dz < \infty\right)$, the boundary effects can be neglected as long as the solution does not broaden too much due to diffusion. This broadening can be avoided by setting the simulation time to a value small

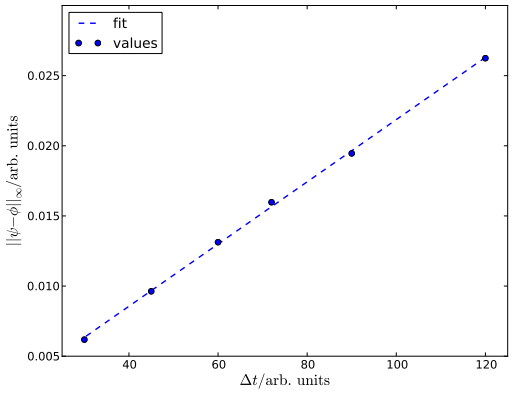

(a) Convergence in time, a linear curve was used to fit the values.

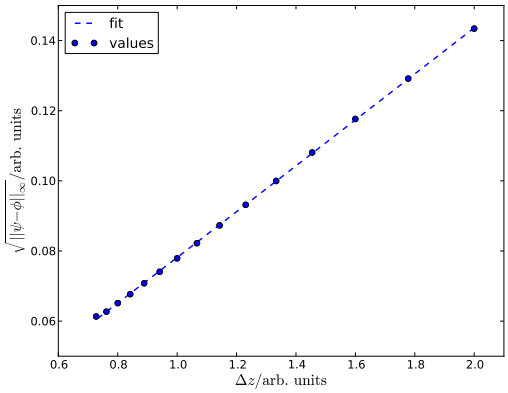

(b) Convergence in depth, a parabolic curve was used to fit the values.

Figure 4.2: The fitted values obtained by a convergence analysis.

enough which means that the simulation stops before a non-zero value of concentration is calculated at the boundaries. Furthermore, numerical schemes cannot deal with delta-peaks which is the initial condition needed for the analytical solution. To deal with this, the analytical solution at a certain point in time $t_0 > 0$ can be used as a new initial condition. With the offset t_0 in time these two solutions can then be compared. Figure 4.1 shows the initial condition used for the simulation and both the analytical and the numerical solution for a specific set of parameters.
The plots of a convergence analysis for the spatial and time discretisation are shown in figures 4.2a and 4.2b. The numerical scheme has a convergence order of $(1, 2)$ in time and space. This result can be extracted from the properties of the graphs used to fit the points in the figures 4.2a and 4.2b. The same order of convergence can be derived mathematically for the numerical schemes of the original one-dimensional equations used by the original GOTM. Thus, the introduction of the horizontally averaged transport equations does not change the order of convergence.
It was checked that the total amount of tracer is conserved by means of equation (3.50) which is the case.

4.1.2 Testing inflows

The inflows were tested with a very simple and unrealistic model setup. A linearly increasing hypsography modulated with a relatively small random signal represents a simple basin. As an initial condition for the salinity, a strongly stratified salt distribution with a small and well mixed bottom boundary layer and a larger surface mixed layer was prescribed. The initial temperature profile consisted of two well mixed layers with a strong thermocline in the upper part of the water column. An inflow with constant volume flow, salinity, and temperature, respectively was prescribed in a way that the density of the inflowing water was high enough to flow into the deeper parts of the modelled basin. The inflowing water was very cold compared to the water column. The total mass of salt contained in this inflow can easily be calculated and could therefore be compared to the total mass of salt being calculated by the numerical model. The eddy diffusivities were computed by means of a k-ϵ turbulence closure model.

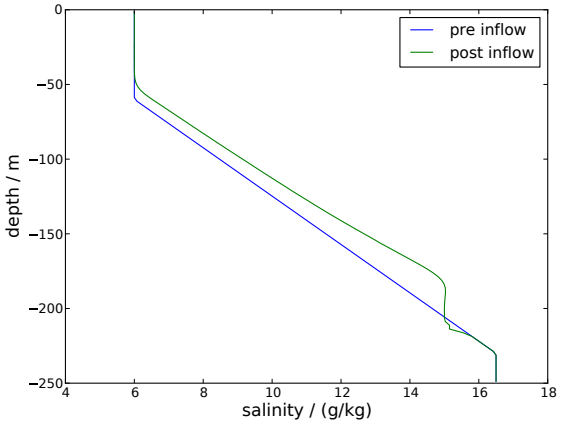

(a) Two salinity profiles, one before the inflow took place and one after the inflow.

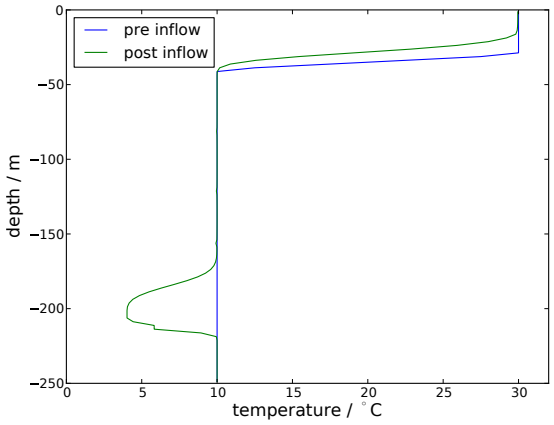

(b) Two temperature profiles, one before the inflow took place and one after the inflow.

Figure 4.3: The effects of a warm and salty inflow on the salinity and temperature profile.

Figure 4.3 shows salinity and temperature profiles before and after the inflow event. In figure 4.3a it can be seen that in a depth of about 200 m a strong jump of salinity formed due to the inflow event. From this depth on upwards, the salinity has increased up until the surface mixed layer due to an advective transport, caused by the inflow which lifted the water up from above the depth of where the inflow spread out into the basin. In figure 4.3b it can be seen that the cold inflowing water pushed the old residing water up and also lifted up the thermocline. Due to the greater density of the newly arrived cold water, the patch of cold water settled stably in the water column. The minor bumps in the profiles are effects arising from the small random "fluctuations" in the hypsography. The increase of the total salt mass in the basin was exactly as much as one would expect from analysing the prescribed values of the inflow. One problem of the inflow algorithm can be seen in figure 4.3a. Directly beneath the depth of where the inflow entered the basin, a minor decrease of salinity was computed. This decrease only appears if the uplifting of the upper water masses by an advective transport is included. The advective and diffusive routines of GOTM are separated from each other. But the advective routine calculates the uplift of the residing salt and the diffusive routine calculates the source of newly arriving salt. Due to this splitting and the sudden increase of the advection velocity, minor discretisation errors occurred. But the inflow simulated here was more intense (a strong volume flow in a short time) than they normally occur in nature which was checked for the Gotland Basin. The less intense an inflow the smaller the errors. Thus, it should not be a problem in realistic model setups.

4.2 An alternative discretisation

The advantage of using equation (3.17)

$$\frac{\partial \phi}{\partial t} = \frac{\partial}{\partial z}\left(\kappa \frac{\partial \phi}{\partial z}\right) - \frac{\partial}{\partial z}\left(\left\{\frac{\mathrm{d}A}{\mathrm{d}z}\frac{\kappa}{A} + w\right\}\phi\right) + \frac{\mathrm{d}A}{\mathrm{d}z}q$$

is that it can easily be integrated into existing models because the diffusion and advection routines do not have to be altered. For this very reason this approach was chosen at first. For every variable being transported, a transformation $\phi(t) = A\varphi(t)$ has to be performed

every time step. This new variable can be processed by already existing diffusion and advection routines. Afterwards, a reverse transformation $\varphi(t + \Delta t) = \phi(t + \Delta t)/A$ has to be applied to obtain meaningful variables again which can be further processed and finally get saved as an output. The idealised test case described in previous section 4.1 gives the same results for this approach. The problems arise when more sophisticated setups are simulated. More precisely, when boundary conditions have to be formulated in combination with unstable stratification causing turbulence. The correct Neumann-type boundary conditions are

$$\kappa \frac{\partial \phi}{\partial z} - \left(\frac{\mathrm{d}A}{\mathrm{d}z} \frac{\kappa}{A} + w \right) \phi = F_s \quad \text{for } z = \zeta \,, \tag{4.1}$$

$$\kappa \frac{\partial \phi}{\partial z} - \left(\frac{\mathrm{d}A}{\mathrm{d}z} \frac{\kappa}{A} + w \right) \phi = F_b \quad \text{for } z = -H \,. \tag{4.2}$$

But if the advective and diffusive parts of the transport equation (3.17) are solved separately, the boundary conditions for the diffusive part are

$$\kappa \frac{\partial \phi}{\partial z} = F_s^d \quad \text{for } z = \zeta \,, \tag{4.3}$$

$$\kappa \frac{\partial \phi}{\partial z} = F_b^d \quad \text{for } z = -H \,, \tag{4.4}$$

and for the advective part

$$-\frac{\mathrm{d}A}{\mathrm{d}z} \frac{\kappa}{A} - w\phi = F_s^a \quad \text{for } z = \zeta \,, \tag{4.5}$$

$$-\frac{\mathrm{d}A}{\mathrm{d}z} \frac{\kappa}{A} - w\phi = F_b^a \quad \text{for } z = -H \,. \tag{4.6}$$

The problem caused by these differences can be illustrated by an example. Imagine a situation where salt is not able to settle on the bottom and no fresh water sources are available at the sea surface, meaning that there is, e.g. no rain. In this scenario the total mass of salt is conserved. But during one time step, in the simulation of this scenario, a certain amount of salt can be transported "into" the boundary by a diffusive transport and at the same time step it can be advected back into the water column again. This can of course also happen by first advecting salt out of the water column and diffusing it back in again. This behaviour can be expressed as

$$F_s^d = -F_s^a \tag{4.7}$$

$$F_b^d = -F_b^a \,. \tag{4.8}$$

If the boundary fluxes are set to zero independently for the diffusive and advective terms the conditions (4.7) and (4.8) are fulfilled although this drastically reduces the solution set of these equations. Several attemps were made to compensate one flux with the other, but no satisfying solution was found.
The effects of the insufficient boundary conditions on the simulation can be seen in strong jumps in the tracer concentrations φ around the boundaries. These jumps can cause

unrealistically unstable stratifications. In combination with the turbulence calculations these instabilities can cause the complete simulation to become unstable. All this does normally not happen, because the resulting effects are negligibly small. But due to the transformation $\phi(t) = A\varphi(t)$ the numerical values of the involved variables ϕ are by several magnitudes greater than the variables φ, which are normally calculated and the errors do not get compensated by the inverse transformation.
Figure 4.4 shows what happens if no flux boundary conditions are applied to a setup in which the salinity has a constant value of $S = 10\,\mathrm{g/kg}$ over the whole water column. It should be noted that in spite of the strong jumps at the boundaries the total salt mass is still conserved up until the uncertainty of the floating number represention of the used computer. No turbulence was applied for these simulations, instead, a constant diffusivity was prescribed.

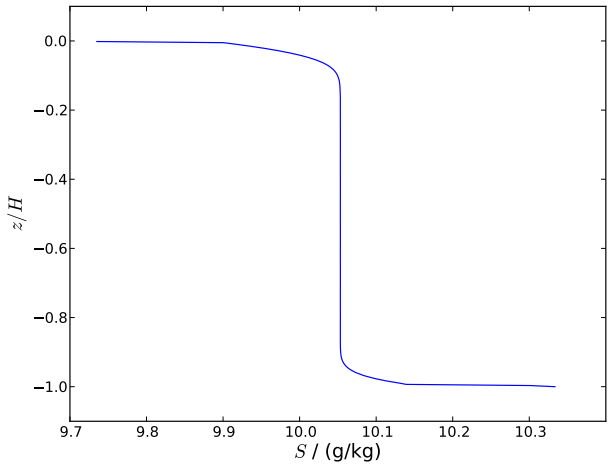

Figure 4.4: The strong jumps are the consequence of the insufficient formulation of the boundary conditions. The initial distribution of the salinity was a constant value of $S = 10\,\mathrm{g/kg}$. Despite these jumps, the total mass of the salt is conserved.

4.3 Simulating the Gotland Basin

4.3.1 Description of the model setup

Before the model setup for the Gotland Basin will be described, the different criteria introduced in section 3.5 will be applied to the Gotland Basin to see if a one-dimensional model is a sufficient way to describe its dynamics.
The atmospheric forcing does not influence the vertical water circulation in the deeper parts of the water column, i.e. beneath the halocline which was the focus of this simulation. Furthermore, following both *Mohrholz* (1998); *Omstedt* (1990) one can assume that the horizontal scales of the atmospheric forcing are larger than the whole Baltic Sea. Differential heating can be neglected, because there simply are no areas shallow enough for this effect to take place in the Gotland Basin.
Assuming an inflow velocity of $u = 6\,\mathrm{cm/s}$, which is two times greater than estimates made by *Hagen and Feistel* (2004), the internal Froude number was always $F_I < 0.7$ for the setup of the Gotland Basin which means that the inertial forces induced by the inflows

get balanced fast enough by the pressure gradient forces to not create strong horizontal inhomogeneities. The relatively fast balancing is important, because these inflows also take place in the deep parts of the Gotland Basin. Evaluating the effects of the outflows on the horizontal water structure is difficult, because the basin is only enclosed up to a water depth of about 140 m. If it is assumed that the hypsography of the Gotland Basin does not increase passed the water depth of 140 m, then the internal Froude number can reach values as high as $F_O = 1.7$. But the outflows take place in the upper layers of the water column which are not constrained by the topography at all, so they belong to the open Baltic Sea. On the one hand, this makes the application of the criteria of the internal Froude number for outflows doubtful for the Gotland Basin. On the other hand, like stated before, this work focusses on the dynamics of the deeper part of the Gotland Basin, which does not get influenced by the outflows, as they are a consequence of the inflows reaching the basin in greater depths.
In the Baltic Sea, the internal Rossby radius has a magnitude of $R_I \approx 5\,\text{km}$. Hence, even for the shortest distance across the Gotland Basin of about $B \approx 40\,\text{km}$ the Coriolis force has a major influence on the dynamics of the Gotland Basin, because of $R = R_I/B = 0.125 < 1$. But the results of a highly time-resolved long-term mooring in the Gotland Basin in combination with the application of a horizontally averaged one-dimensional model show that the basin wide eddy diffusivities react in time scales of several days to storm events (*Holtermann and Umlauf*, 2012). Together with the fact that mixing in the Gotland Basin is boundary dominated (*Holtermann et al.*, 2012), this means that the interior water homogenises with the mixed water at the boundaries within a period of a few weeks. The isopycnal homogenisation is influenced and probably increased by processes such as subinertial topographic waves or internal waves which are motions affected by the Coriolis force. Because of the fast homogenisation, the Coriolis force should not break the assumptions made for a one-dimensional model.

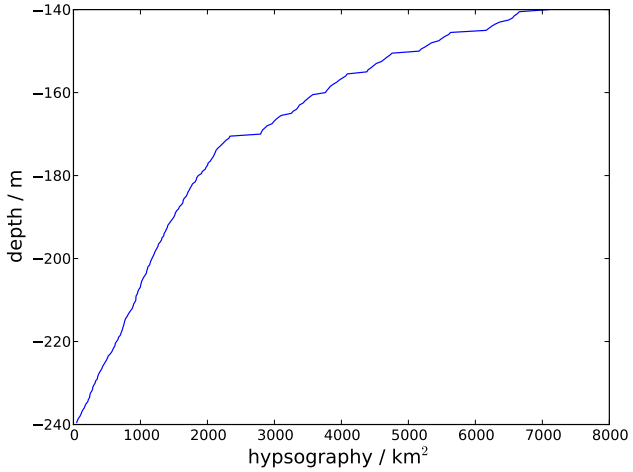

Figure 4.5: The hypsographical function of the Gotland Basin up to a water depth of 140 m where the basin is not enclosed anymore.

In a nutshell, some problems could arise due to the use of a one-dimensional model, but so would the use of a three-dimensional model have its own problems. Therefore, this sections concludes that modelling the Gotland Basin with a one-dimensional water column model

seems promissing especially if one considers that the main view lies on the dynamics in the deeper parts of the Gotland Basin.
Thus, the Gotland Basin was simulated over a period of seven years from the 1 January 2003 until 1 January 2010 with a time step of $\Delta t = 10\,\text{min}$. The simulation of the basin already started on 1 October 2002, but the inflows were only included from 1 January 2003 on. During this simulation period one major Baltic inflow occurred in January 2003 which arrived at the bottom of the Gotland Basin in May (*Feistel et al.*, 2003). After this event a prolonged period of stagnation began with only a few minor inflows of which non had a significant impact on the conditions at the bottom of the Gotland Basin (*Nausch et al.*, 2011).
The eddy diffusivities were calculated by means of a k-ϵ turbulence closure model. The hypsographical data was extracted from bathymetrical data compiled by *Seifert et al.* (2001) and the meteorological data used for the atmospherical forcing like the wind speed, the air pressure, the air temperature, and so on were taken from *Saha et al.* (2010). The hypsographical function of the Gotland Basin is shown in figure 4.5.

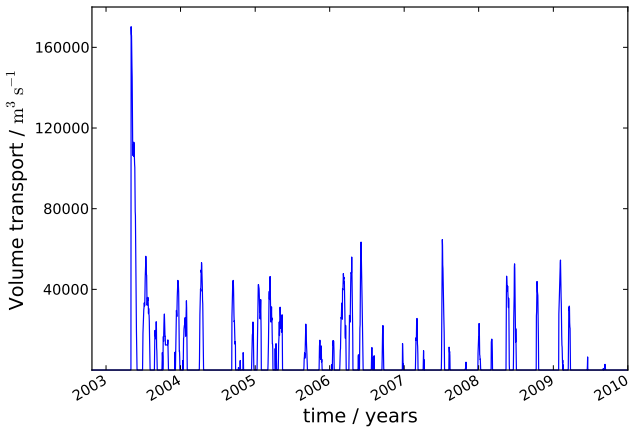

Figure 4.6: The inflows used to force the model. The strong peak in early 2003 marks the major Baltic inflow discussed, e.g. by *Feistel et al.* (2003, 2006).

Unfortunately no data was available to realistically prescribe inflows. Therefore, data from a simulation run with a three-dimensional circulation model of the western Baltic Sea was used for prescribing the inflows. This data was gained by means of the General Estuarine Transport Model (GETM) with a resolution of 600 m (*Gräwe et al.*, 2012). A transect across the Arcona Basin was used to calculate the inflows passing this basin. The volume transport was computed by integrating the flow velocities perpendicular to the transect. This volume transport, the salinity, and the temperature of the inflowing water in the Arcona Basin where used together with the entrainment equations derived in section 3.3 to obtain the properties of the deep water currents entering the Gotland Basin. These properties where then used to force the model. Figure 4.6 shows the volume of water being transported into the Gotland Basin. The average transport is $\bar{Q} = 6000\,\text{m}^3\text{s}^{-1}$. A constant brackish water inflow at the sea surface with a salinity of 5.6 g/kg, which is the long-term mean salinity of the surface water in the basins north of the Gotland Basin (*Axell*, 2002), was added to incorporate the river runoff. The volume flow was set to $1200\,\text{m}^3\text{s}^{-1}$.

The observed data to which the simulation results are compared to and which were used as hydrological initial conditions were obtained from a database called DAS (*Sokolov et al.*, 1997). The database contains raw data which was not checked for plausibility. Therefore, some filters were applied to the data to at least remove the obvious measuring errors.

4.3.2 Discussion of the results

Figure 4.7 shows a comparison of the simulation results with observed data of the salinity and the temperature of the Gotland Basin. The pronounced and permanent halocline can be seen in the salinity plots and the summer warming and winter cooling of the surface layers can be clearly seen in the temperature plots. It can also be seen that the simulated halocline is 10 m to 20 m too high in the water column and that the observed halocline is sharper then the simulated one. The depth difference can be explained by the way the outflows are modelled. The water masses, which are pushed upwards due to an inflow, reach all the way up to the surface where they are treated as an outflow. This is most likely not what happens in the Gotland Basin as it is only enclosed up to a water depth of 140 m. From this depth on, the water can also spread laterally and thus will not push the halocline upwards in such a way. This inaccuracy of the model has another consequence. From the time on, the major Baltic inflow occurred, the surface salinity is too high due to smaller inflows pushing up the water masses from depths of about the halocline, see figure 4.8a for a more detailed view. These, in comparison to the surface water, relatively saline water masses also end as an outflow at the upper most water layers and therefore increase the salinity at the surface.
Another discrepancy between the observations and the simulation results is the temperature of the deep Gotland Basin. This discrepancy can be seen more clearly in figure 4.8b. Not only does the simulated initial inflow cool the Gotland Basin by 2 °C more than the measurements indicate, but the data used to force the inflows obviously does not include the warm baroclinic inflow in August 2003 (*Feistel et al.*, 2006), which can also be seen in figure 4.6, where there are no significant peaks around this time. Figure 4.8b shows that due to this warm inflow the bottom part of the basin warmed up to similar values as before the cold inflow of spring 2003. The 2 °C too cold inflowing water can also only be explained by inconsistences in the data used to prescribe inflows because it was checked that the entrainment could not have cooled the water so drastically.
The surface temperature was reproduced in good accordance with the observations which can be seen in figure 4.8c. The discrepancies, especially in the summer months, are mainly due to large temporal gaps in the observations. The bottom salinity dynamics are also reproduced in agreement with the observations, see figure 4.8d. Although the highest salinity is only reached gradually and the simulation predicts a sudden increase to the highest values of salinity the slow decline of the salinity is in good accordance with the measurements.
From figure 4.9a, it can be seen that the salinity profile is reproduced in a satisfying way before the major Baltic inflow occurs, whereas the profiles after a prolonged stagnation period on 18 September 2008 (figure 4.9b) show significant discrepancies. The salinity in the deepest parts of the Gotland Basin was reproduced well, as already seen in figure 4.8d, but above that, in depths between 120 m and 200 m, the salinity is underestimated. This underestimation could arise from some subsequent smaller inflows following the major one in spring 2003, like the warm inflow in August 2003, which was not included in the data used for the simulation of the inflows.

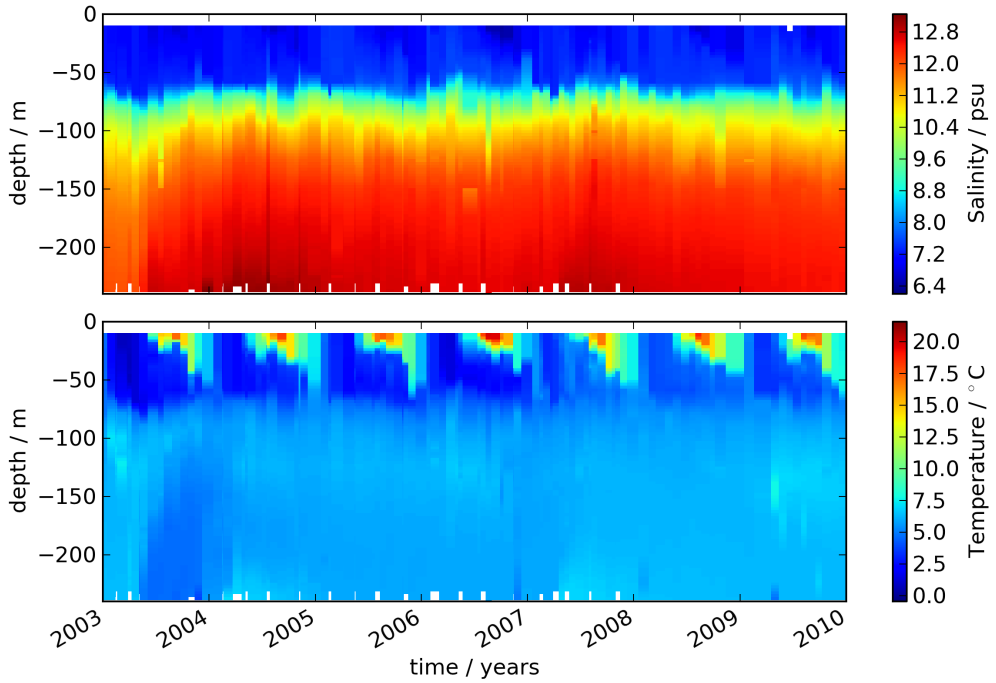

(a) Observations of salinity and temperature in the Gotland Basin.

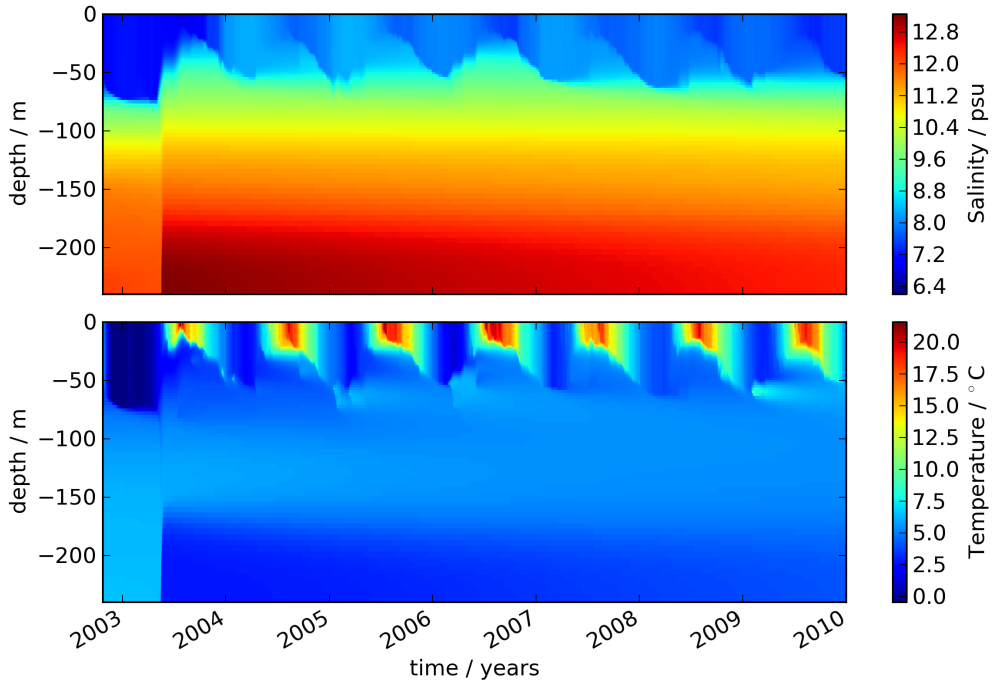

(b) Results of the simulation for salinity and temperature.

Figure 4.7: A comparison of the simulation results to the observations made in the Gotland Basin.

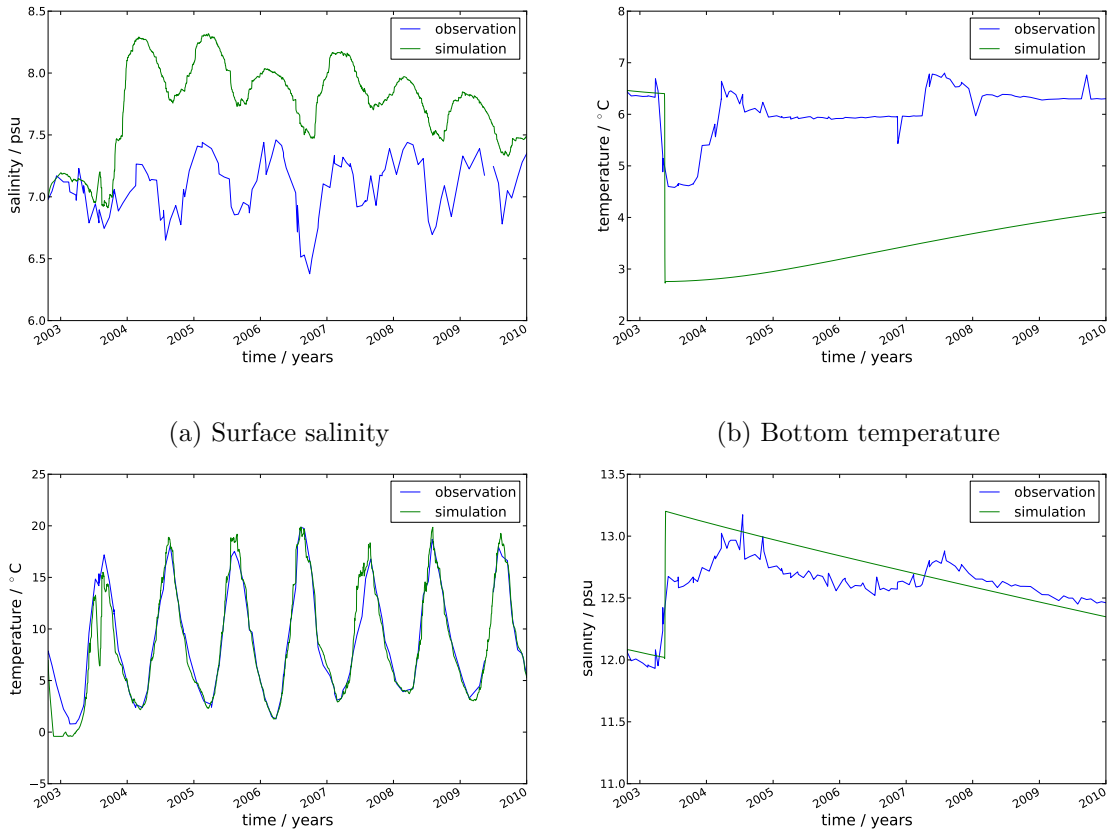

(a) Surface salinity

(b) Bottom temperature

(c) Surface temperature

(d) Bottom salinity

Figure 4.8: Time series of the salinity (a) and temperature (b) dynamics in the deep parts (220 m) of the Gotland Basin. The strong jumps in both the salinity and the temperature time series mark the major Baltic inflow of early 2003. The salinity and temperature in the surface mixed layer (20 m) are shown in figures (c) and (d) respectively.

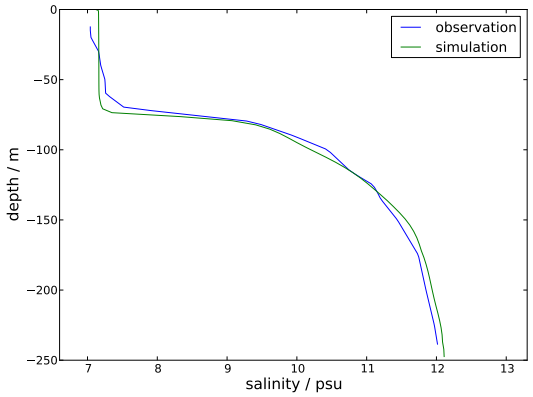

(a) Salinity profile on 20 February 2003

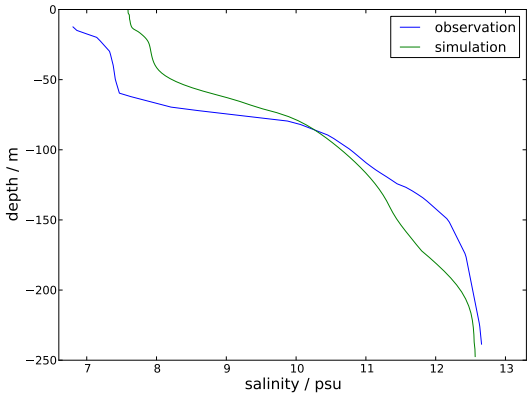

(b) Salinity profile on 10 July 2008

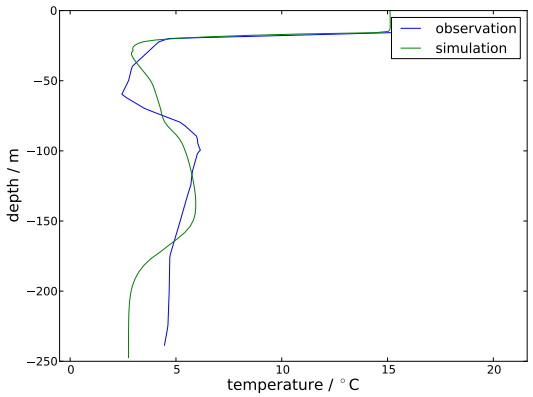

(c) Temperature profile on 27 August 2003

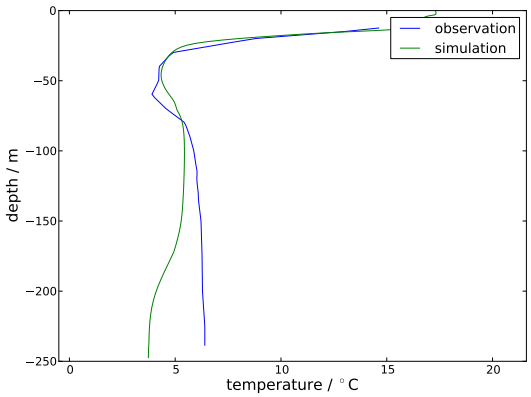

(d) Temperature profile on 10 July 2008

Figure 4.9: Profiles of the salinity before the major Baltic inflow (a) and after a prolonged stagnation period (b) and temperature profiles after the major Baltic inflow (c) and after a stagnation period (d).

Figures 4.9c and 4.9d show that the temperature profiles can be reproduced up until a depth depending on how long the major Baltic inflow from 2003 is already past, as the too cold deep parts of the Gotland Basin gradually influence the upper parts of the water column by cooling them.
To summerise this discussion, the observations could be reproduced qualitatively in nearly all aspects with the deep temperature dynamics being the exception. Furthermore, the surface temperature and the bottom salinity could be reproduced quantitatively. The reasons for discrepancies between the observations and the simulation come down to two problems. First, the data used to calculate the inflows came from a simulation run which obviously has its own flaws and second, the outflow of the uplifted water masses is poorly modelled.

Chapter 5

Conclusions

A horizontally integrated one-dimensional hydrodynamical model was derived and implemented into the already existing General Ocean Turbulence Model. The dynamic equations of this model not only include effects induced by the hypsography of the simulated basin, but also give the ability to include inflows at arbitrary water depths and to account for the resulting vertical transports. An analytical solution was found which satisfies the newly derived equations. The numerical implementation of these equations could therefore be tested against this solution and that with good results. A first approach to discretising the dynamic equations failed, because the splitting of the advection and diffusion scheme resulted in an insufficient formulation of the boundary conditions for the transport of a tracer (e.g. salt or heat). This discretisation is more elegant with respect to the implementation, as it allows to reuse already written and tested numerical schemes. But this approach was abandoned and instead the numerical schemes were adapted to the horizontally integrated equations. Furthermore, an entrainment model was introduced which makes it possible to include inflows measured or simulated far away from the actual simulated basin. These inflows could come from a river in the case of a simulated lake or like in the case of this thesis they could be dense bottom currents entering a sub-basin of the Baltic Sea. The entrainment model together with the extended version of GOTM was finally used to simulate the Gotland Basin over a time period of seven years. During this period one major Baltic inflow occurred. The comparison of the simulation results with measured data showed that the hydrodynamics of the Gotland Basin could be reproduced qualitatively. Some aspects of the hydrodynamics of the basin could even be reproduced quantitatively in a very satisfying way. If some behaviour or property could not be reproduced satisfyingly, then reasons for this inability could be found. If more time would be spent tweaking parameters for the Gotland Basin and, more importantly, if the model would be refined to consider the fact that the Gotland Basin is only enclosed up until a water depth of 140 m, then the results should be significantly better. The refinement of the model would include brackish outflows from 140 m on upwards and thus, not pushing the halocline so far upwards. A minor discretisation error, which was found with the help of idealised inflow simulations, could possibly be significantly reduced, if higher order advection schemes would be implemented for the horizontally averaged version of the advection equation. Another problem of the simulation runs was the data from the Arcona Basin which was used to calculate the inflows into the Gotland Basin. This data had to be taken from a simulation performed with a three-dimensional circulation model because observations were not available. If measurements could have been taken, then the simulation of the Gotland Basin would have certainly given better results, as, e.g. the important

warm inflow in August 2003 was not reproduced by the simulation used for prescribing the inflows. The Gotland Basin is a very complex and complicated hydrodynamical system and the fact that the inflows were precribed over 600 km further upstream does not make the task of modelling the Gotland Basin easier. Thus, the model, as it is, will most likely give even better results for systems with more simple hydrodynamics. In the scope of this thesis it could not be tested elaborately how well the entrainment model performed, but *Stigebrandt* (1987) showed that the entrainment model gives satisfying results for synthetically generated inflow properties which have the same statistical properties as observed inflows. Of course, this excludes month-to-month comparisons with observations.
The extended version of GOTM, which was developed in the course of this thesis, was published under the GNU General Public License (GPL) and can be found under `www.gotm.net` in the "lake" branch of the source code repository. For only browsing the source code following web page is recommended: `http://sourceforge.net/projects/gotm/`. Without any modifications the model can be used for simulating lakes or sub-basins of oceans. For simulating a lake, the entrainment model can be fully omitted and the river discharge together with the temperature of the river water can be prescribed. The original version of GOTM can be coupled to biogeochemical models. In principle, this coupling is also possible for the horizontally integrated version of GOTM, but the transport equations for the biological state variables have to be horizontally integrated first.
In a nutshell, the horizontally integrated version of GOTM could become an important tool for not only studying hydrodynamic processes in lakes and ocean basins, but also for calibrating parameters in a very short time compared to other models. The last point could be even more important for coupled physical-biogeochemical models because the amount of parameters which need to be adjusted increases a lot for such coupled models.

Bibliography

Axell, L. B. (2002), Wind-driven internal waves and Langmuir circulations in a numerical ocean model of the southern Baltic Sea, *J. Geophys. Res.*, *107*(C11), 3204.

Bronstein, I., and K. Semendjajew (2005), *Taschenbuch der Mathematik*, Harri Deutsch GmbH.

Burchard, H., and K. Bolding (2001), Comparative analysis of four second-moment turbulence closure models for the oceanic mixed layer, *J. Phys. Oceanogr.*, *31*, 1943–1968.

Burchard, H., H. U. Lass, V. Mohrholz, L. Umlauf, J. Sellschopp, V. Fiekas, K. Bolding, and L. Arneborg (2005), Dynamics of medium-intensity dense water plumes in the Arkona Sea, Western Baltic Sea, *Ocean Dyn.*, *55*, 391–402.

Burchard, H., K. Bolding, W. Kühn, A. Meister, T. Neumann, and L. Umlauf (2006), Description of a flexible and extendable physical-biogeochemical model system for the water column, *J. Mar. Sys.*, *61*, 180–211.

Burchard, H., F. Janssen, K. Bolding, L. Umlauf, and H. Rennau (2009), Model simulations of dense bottom currents in the Western Baltic Sea, *Cont. Shelf Res.*, *29*, 205–220.

Canuto, V. M., A. Howard, Y. Cheng, and M. S. Dubovikov (2001), Ocean turbulence. Part I: One-point closure model—Momentum and heat vertical diffusivities, *J. Phys. Oceanogr.*, *31*, 1413–1426.

Feistel, R., G. Nausch, W. Matthäus, and E. Hagen (2003), Temporal and spatial evolution of the Baltic deep water renewal in spring 2003, *Oceanologica*, *45*, 623–642.

Feistel, R., et al. (2004a), Background data to the exceptionally warm inflow into the Baltic Sea in late summer of 2002, *Marine Science Reports*, *58*, 1–58.

Feistel, R., G. Nausch, T. Heene, J. Piechura, and E. Hagen (2004b), Evidence for a warm water inflow into the Baltic Proper in summer 2003, *Oceanologica*, *46*, 581–598.

Feistel, R., G. Nausch, and E. Hagen (2006), Unusual Baltic inflow activity in 2002-2003 and varying deep-water properties, *Oceanologia*, *48*(S), 21–35.

Feistel, R., S. Feistel, G. Nausch, J. Szaron, Lysiak-Pastuszak, E., and G. Aertebjerg (2008), BALTIC: Monthly time series 1900-2005, in *State and Evolution of the Baltic Sea 1952-2005*, edited by R. Feistel, G. Nausch, and N. Wasmund, pp. 11–336, John Wiley & Sons, Hoboken, New Jersey.

Fofonoff, N. P., and R. C. Millard (1983), Algorithms for the computation of fundamental properties of seawater, *UNESCO technical papers in marine sciences*, *44*, 1–53.

Gräwe, U., H. Burchard, P. Holtermann, K. Klingbeil, and H. Siegel (2012), Assessing the skill of a triple nested hydrodynamic model of the coupled system north sea - baltic sea, *Continental Shelf Research*, in preparation.

Hagen, E., and R. Feistel (2001), Spreading of Baltic deep water: A case study for the winter 1997-1998, *Marine Science Reports*, *45*, 99–133.

Hagen, E., and R. Feistel (2004), Observations of low-frequency current fluctuations in deep water of the Eastern Gotland Basin/Baltic Sea, *J. Geophys. Res.*, *109*, C03,044.

HELCOM (1993), First assessment of the state of the coastal water of the baltic sea, *Baltic Sea Environment Proceedings*, *54*.

Holtermann, P. L., and L. Umlauf (2012), The baltic sea tracer release experiment: 2. mixing processes, *J. Geophys. Res.*, *117*, C01,022.

Holtermann, P. L., L. Umlauf, T. Tanhua, O. Schmale, G. Rehder, and J. J. Waniek (2012), The baltic sea tracer release experiment: 1. mixing rates, *J. Geophys. Res.*, *117*, C01,021.

IOC, SCOR, and IAPSO (2010), The international thermodynamic equation of seawater - 2010: Calculation and use of thermodynamic properties, *Intergovernmental Oceanographic Commision, Manuals and Guides No.*, *56*, 196pp, UNESCO (English).

Jöhnk, K. (2000), 1D Hydrodynamische Modelle in der Limnophysik. Turbulenz-Meromixis-Sauerstoff., *Habilitation thesis*, Department of Mechanics, Technical University at Darmstadt, Germany, in German.

Jöhnk, K., and L. Umlauf (2001), Modelling the metalimnetic oxygen minimum in a medium sized alpine lake, *Ecol. Model.*, *136*, 67–80.

Kato, H., and O. M. Phillips (1969), On the penetration of a turbulent layer into stratified fluid, *J. Fluid Mech.*, *37*(4), 643–655.

Kundu, P. K., and I. M. Cohen (2008), *Fluid Mechanics*, 4$^{\text{th}}$ ed., 872 pp., Academic Press, London, UK.

Lass, H. U., and V. Mohrholz (2003), On dynamics and mixing of inflowing saltwater in the arkona sea, *J. Geophys. Res.*, *108*, 3042pp.

Lass, H. U., V. Morhholz, and T. Seifert (2005), On pathways and residence time of salt-water plumes in the Arkona Sea, *J. Geophys. Res.*, *110*, C11,019.

Liljebladh, B., and A. Stigebrandt (1996), Observations of the deepwater flow into the Baltic Sea, *J. Geophys. Res.*, *101*(C4), 8895–8911.

Matthäus, W., and H. Franck (1992), Characteristics of major Baltic inflows - a statistical analysis, *Cont. Shelf Res.*, *12*(12), 1375–1400.

Matthäus, W., R. Feistel, H.-U. Lass, G. Nausch, D. Nehring, and V. Mohrholz (2008), The inflow of highly saline water into the Baltic Sea, in *State and Evolution of the Baltic Sea 1952-2005*, edited by R. Feistel, G. Nausch, and N. Wasmund, pp. 65–309, John Wiley & Sons, Hoboken, New Jersey.

Meier, H. E. M., et al. (2006), Ventilation of the Baltic Sea deep water: A brief review of present knowledge from observations and models, *Oceanologia*, *48*, 133–164.

Mohrholz, V. (1998), Transport- und Vermischungsprozesse in der Pommerschen Bucht, *Marine Science Reports*, *19*, 106pp.

Nausch, G., R. Feistel, and V. Mohrholz (2011), Water exchange between the baltic sea and the north sea, and conditions in the deep basins, HELCOM Indicator Fact Sheets 2011, online, 2012 January 15, http://www.helcom.fi/environment2/ifs/en_GB/cover/.

Omstedt, A. (1987), Water cooling in the entrance of the Baltic Sea, *Tellus*, *39A*(3), 254–265.

Omstedt, A. (1990), Modelling the Baltic Sea as thirteen sub-basins with vertical resolution, *Tellus*, *42A*(2), 286–301.

Oreskes, N., K. Shrader-Frechette, and K. Belitz (1994), Verification, validation, and confirmation of numerical models in the earth sciences, *Science*, *263*(5147), 641–646.

Patterson, J. C., P. Hamblin, and J. Imberger (1984), Classification and dynamic simulation of the vertical density structure of lakes, *Limnol. Oceanogr.*, *29*(4), 845–861.

Pope, S. B. (2000), *Turbulent Flows*, 806 pp., Cambridge University Press, Cambridge, UK.

Reissmann, J., H. Burchard, R. Feistel, E. Hagen, H.-U. Lass, V. Mohrholz, G. Nausch, L. Umlauf, and G. Wieczorek (2009), Vertical mixing in the Baltic Sea and consequences for eutrophication - A review, *Progr. Oceanogr.*, *82*(1), 47–80.

Saha, S., et al. (2010), The ncep climate forecast system reanalysis, *Bulletin of the American Meteorological Society*, *91*(8), 1015–1057.

Seifert, T., F. Tauber, and B. Kayser (2001), A high resolution spherical grid topography of the baltic sea - 2nd edition, in *Proceedings of the Baltic Sea Science Congress*, Poster #147, www.io-warnemuende.de/iowtopo.

Sellschopp, J., L. Arneborg, M. Knoll, V. Fiekas, F. Gerdes, H. Burchard, U. Lass, V. Mohrholz, and L. Umlauf (2006), Direct observations of a medium-intensity inflow into the Baltic Sea, *Cont. Shelf Res.*, *26*(19), 2393–2414.

Sokolov, A., O. Andrejev, F. Wulff, and M. R. Medina (1997), The Data Assimilation System for Data Analysis in the Baltic Sea, in *Systems Ecology Contributions, 3*, p. 66pp, Stockholm University.

Speziale, C. G. (1991), Analytical methods for the development of Reynolds-stress closures in turbulence, *Ann. Rev. Fluid Mech.*, *23*, 107–157.

Stigebrandt, A. (1985), A model for the seasonal pycnocline in rotating systems with application to the Baltic Proper, *J. Phys. Oceanogr.*, *15*, 1392–1404.

Stigebrandt, A. (1987), A model for the vertical circulation of the Baltic deep water, *J. Phys. Oceanogr.*, *17*(10), 1772–1785.

Stigebrandt, A. (2001), Physical Oceanography of the Baltic Sea, in *A Systems Analysis of the Baltic Sea*, edited by F. Wulff, L. Rahm, and P. Larsson, pp. 19–68, Springer, Berlin.

Stigebrandt, A., and F. Wulff (1987), A model for the dynamics of nutrients and oxygen in the Baltic proper, *J. Mar. Res.*, *45*, 729–759.

Umlauf, L., and H. Burchard (2005), Second-order turbulence closure models for geophysical boundary layers. A review of recent work, *Cont. Shelf Res.*, *25*, 795–827.

Umlauf, L., H. Burchard, and K. Hutter (2003), Extending the k-ω turbulence model towards oceanic applications, *Ocean Modelling*, *5*, 195–218.

Umlauf, L., H. Burchard, and K. Bolding (2005), GOTM – Scientific Documentation. Version 4.0, *Marine Science Reports 63*, Leibniz-Institute for Baltic Sea Research, Warnemünde, Germany.

Umlauf, L., L. Arneborg, H. Burchard, V. Fiekas, H.-U. Lass, V. Mohrholz, and H. Prandke (2007), Transverse structure of turbulence in a rotating gravity current, *Geophys. Res. Lett.*, *34* (L08601).

Eidesstattliche Erklärung

Ich versichere eidesstattlich durch eigenhändige Unterschrift, dass ich die Arbeit selbständig und ohne Benutzung anderer als der angegebenen Hilfsmittel angefertigt habe. Alle Stellen, die wörtlich oder sinngemäß aus Veröffentlichungen entnommen sind, habe ich als solche kenntlich gemacht.

Ort, Abgabedatum	Unterschrift